1 *In vivo* human neurite exchange imaging

2 (NEXI) at 500 mT/m diffusion gradients

3 Neurite exchange time imaging on Connectome 2.0

4

5 [Authors]

6 [1,2]Kwok-Shing Chan, PhD, kchan2@mgh.harvard.edu

7 [1,2]Yixin Ma, PhD, YMA12@mgh.harvard.edu

8 [1,2]Hansol Lee, PhD, HLEE89@mgh.harvard.edu

9 [3]José P. Marques, PhD, jose.marques@donders.ru.nl

10 [4,5]Jonas Olesen, PhD, jonas@phys.au.dk

11 [6,7]Santiago Coelho, PhD, santiago.coelho@nyulangone.org

12 [6,7]Dmitry S Novikov, PhD, dmitry.novikov@nyulangone.org

13 [4,5]Sune Jespersen, PhD, sune@cfin.au.dk

14 [1,2]Susie Y. Huang, MD, PhD, Susie.Huang@MGH.HARVARD.EDU

15 [1,2]Hong-Hsi Lee, MD, PhD, HLEE84@mgh.harvard.edu

16

17 [Affiliations]

18 [1]Athinoula A. Martinos Center for Biomedical Imaging, Charlestown, MA, United

19 States

20 [2]Department of Radiology, Massachusetts General Hospital, Harvard Medical School,

21 Boston, MA, United States

1

Correspondence to Hong-Hsi Lee

22   [3]Donders Institute for Brain, Cognition and Behaviour, Radboud University, Nijmegen,

23   The Netherlands

24   [4]Center of Functionally Integrative Neuroscience (CFIN) and MINDLab, Department

25   of Clinical Medicine, Aarhus University, Aarhus, Denmark

26   [5]Department of Physics and Astronomy, Aarhus University, Aarhus, Denmark

27   [6]Center for Biomedical Imaging, Department of Radiology, New York University

28   School of Medicine, New York, NY 10016, USA

29   [7]Center for Advanced Imaging Innovation and Research (CAI2R), Department of

30   Radiology, New York University School of Medicine, New York, NY 10016, USA

31

32   [Correspondence to]

33   Hong-Hsi Lee, MD, PhD, HLEE84@mgh.harvard.edu

34   Athinoula A. Martinos Center for Biomedical Imaging, Charlestown, MA, United States

35   149 13th St, Charlestown, MA, USA

36

39

40   [Highlights]

41   -   The Connectome 2.0 scanner equipped with 500 mT/m gradients enables high-

42   sensitivity diffusion MRI for imaging exchange times *in vivo*

43   -   The global exchange time across the living human cortex was estimated to be

44   about 13 ms on Connectome 2.0, faster than measured using a protocol

45   compatible to Connectome 1.0

46   -   Spatially varying exchange times were observed across the cortex

2

Correspondence to Hong-Hsi Lee

47   -   A GPU-accelerated tool was developed to speed up parameter estimation by

48   100 times

49   -   The narrow pulse approximation used in neurite exchange imaging does not

50   affect estimation performance in high gradient performance MRI systems

51

3

Correspondence to Hong-Hsi Lee

Abstract

Evaluating tissue microstructure and membrane integrity in the living human brain through diffusion-water exchange imaging is challenging due to requirements for a high signal-to-noise ratio and short diffusion times dictated by relatively fast exchange processes. The goal of this work was to demonstrate the feasibility of *in vivo* imaging of tissue micro-geometries and water exchange within the brain gray matter using the state-of-the-art Connectome 2.0 scanner equipped with an ultra-high-performance gradient system (maximum gradient strength=500 mT/m, maximum slew rate=600 T/m/s). We performed diffusion MRI measurements in 15 healthy volunteers at multiple diffusion times (13-30 ms) and b-values up to 17.5 ms/μm^2. The anisotropic Kärger model was applied to estimate the exchange time between intra-neurite and extracellular water in gray matter. The estimated exchange time across the cortical ribbon was around (median±interquartile range) 13±8 ms on Connectome 2.0, substantially faster than that measured using an imaging protocol compatible with Connectome 1.0-alike systems on the same cohort. Our investigation suggested that the NEXI exchange time estimation using a Connectome 1.0 compatible protocol was more prone to residual noise floor biases due to the small time-dependent signal contrasts across diffusion times when the exchange is fast ($\leq$20 ms). Furthermore, spatial variation of exchange time was observed across the cortex, where the motor cortex, somatosensory cortex and visual cortex exhibit longer exchange times compared to other cortical regions. Non-linear fitting for the anisotropic Kärger model was accelerated 100 times using a GPU-based pipeline compared to the conventional CPU-based approach. This study highlighted the importance of the chosen diffusion times and measures to address Rician noise in dMRI data, which can have a

4

Correspondence to Hong-Hsi Lee

76   substantial impact on the estimated NEXI exchange time and require extra attention

77   when comparing NEXI results between various hardware setups.

78

5

Correspondence to Hong-Hsi Lee

1. Introduction

Understanding the dynamics of water exchange within the human brain provides a key window into deciphering pathological mechanisms and assessing tissue integrity in aging and a variety of neurological and psychiatric disorders (Bai et al., 2019, 2018). In neural tissues, water can passively traverse lipid bilayers or via aquaporins, specialized membrane protein channels that facilitate water movement between extracellular and intracellular compartments (Papadopoulos and Verkman, 2013). Disruptions in water homeostasis in conditions such as brain edema or ischemic stroke may alter membrane permeability between water compartments (King et al., 2004). Recent research has also highlighted the role of ATPase channels in actively co-transporting water for maintaining osmotic balance and supporting normal brain function (MacAulay, 2021; Springer et al., 2023b, 2023a; Williamson et al., 2023). Characterizing membrane permeability may offer new insights into physiological processes and holds promise for disease monitoring and therapeutic intervention (Badaut et al., 2014). By elucidating these mechanisms, researchers can potentially identify novel targets for intervention and refine treatment strategies aimed at preserving brain health.

Diffusion MRI (dMRI) is a versatile imaging modality for investigating brain tissue microstructure noninvasively (Basser, 1997; Le Bihan, 1995). By harnessing magnetic field gradients, dMRI encodes the displacement of water molecules through the signal attenuation incurred as water molecules diffuse randomly and cause irreversible phase dispersion (Carr and Purcell, 1954; Stejskal and Tanner, 1965). In neural tissues, water diffusion is often restricted or hindered by cell membranes and

6

Correspondence to Hong-Hsi Lee

103   organelles (Beaulieu, 2002). Understanding how diffusion-induced signal attenuation

104   varies as a function of diffusion-encoding gradient field strength, duration, and

105   diffusion times with respect to tissue microscopic structure promises to yield valuable

106   histological-level information. One of the most widely applied uses of dMRI is the study

107   of white matter microstructure (Assaf et al., 2008, 2004; Fan et al., 2020; Fieremans

108   et al., 2011; Huang et al., 2020; Jespersen et al., 2007; Kaden et al., 2016; Zhang et

109   al., 2012). The prevailing biophysical model of diffusion in white matter involves a

110   collection of fiber bundles (fascicles), each comprised of aligned anisotropic water

111   compartments with Gaussian diffusion, characterized by distinct diffusivities and water

112   fractions, corresponding to the water inside and outside axons (Novikov et al., 2018b,

113   2019). Due to the presence of myelin sheath, water exchange between the

114   compartments within a bundle is neglected over typically used diffusion times (Nilsson

115   et al., 2013; Veraart et al., 2020, 2019). The orientations of such multicompartmental

116   fiber bundles within a voxel are characterized by a fiber orientation distribution function

117   (ODF). This model, involving both the compartmental parameters of the bundle and

118   the orientational parameters of the ODF, is commonly referred to as the Standard

119   Model of diffusion in white matter (Novikov et al., 2018b, 2019).

120

121   Extending the Standard Model onto gray matter requires accounting for its specific

122   microstructure properties. First, the soma compartment, corresponding to the cell

123   bodies of neurons and glial cells, constitutes a significant portion of the gray matter

124   volume (10-20%) (Shapson-Coe et al., 2024) and has a distinct isotropic and fully

125   restricted contribution to the MRI signal (Palombo et al., 2020). Second, while myelin

126   acts as a major barrier to diffusion and intercompartmental exchange in white matter,

127   its concentration in gray matter is notably lower (Shapson-Coe et al., 2024), though

7

Correspondence to Hong-Hsi Lee

128   both myelinated and unmyelinated axons can coexist in a voxel. The thin, branch-like

129   cellular structures (neurites), such as unmyelinated axons, dendrites and glial cell

130   processes, may contribute to a non-negligible water exchange between neurites and

131   extracellular space across the neurite membrane given the relatively high surface-

132   area-to-volume ratio and/or other water transport mechanisms, such as via aquaporins

133   and ATPase channels (MacAulay, 2021; Papadopoulos and Verkman, 2013; Springer

134   et al., 2023b, 2023a; Veraart et al., 2020; Williamson et al., 2023).

135

136   The presence of intercompartmental water exchange and restricted diffusion can be

137   disentangled through multidimensional spectroscopy methods like diffusion exchange

138   spectroscopy (DEXSY) (Callaghan and Furó, 2004). In DEXSY, water exchange

139   between environments with different diffusivities is observed during the mixing time of

140   a double diffusion encoding scheme, manifesting as off-diagonal elements in the two-

141   dimensional spectrum (Callaghan and Furó, 2004). However, DEXSY demands a

142   large amount of data to compute the multidimensional exchange spectrum, which

143   limits its direct applicability in imaging contexts. Efforts have been made to shorten the

144   lengthy acquisition of DEXSY (Åslund et al., 2009; Cai et al., 2018; Williamson et al.,

145   2020, 2019), notably through filtered exchange imaging (FEXI) (Lasič et al., 2011), a

146   variant tailored for clinical feasibility. Nonetheless, the interpretation of apparent

147   exchange rates derived from FEXI can be confounded by water exchange between

148   the intra- and extra-vascular environments (Bai et al., 2020) and the geometry of the

149   involved compartments (Khateri et al., 2022; Li et al., 2023). Despite the challenges

150   facing FEXI, previous research underscores the association between apparent

151   exchange rates and membrane permeability (Nilsson et al., 2013; Ning et al., 2018).

152

     8

     Correspondence to Hong-Hsi Lee

153   To shorten the lengthy multi-dimensional DEXSY-like experiments, tissue

154   microstructure and intercompartmental water exchange can be assessed by

155   employing a parsimonious *model* of exchange between just a few compartments.

156   Models reduce the number of parameters making their estimation more robust and

157   less SNR-demanding, yet they rely on explicit assumptions for the microstructure

158   (Novikov et al., 2018a). The most widespread model of exchange in the dMRI context

159   has been suggested by Kärger (Kärger, 1985). In its original formulation, exchange

160   was postulated to occur between two isotropic compartments with otherwise Gaussian

161   diffusion, at each point of the sample, governed by simple rate equations in the spirit

162   of (Zimmerman and Brittin, 1957).

163

164   Extending the Kärger model (KM) onto structurally rich microstructure involved

165   clarifying its assumptions. It was realized that KM applies only at sufficiently long

166   diffusion times, after *coarse-graining* the tissue microstructure by the diffusion process,

167   i.e., at the scales exceeding cell sizes and the correlation length l_c of cell packing,

168   assuming that the exchange time $t_{ex} \gg t_c$ is also slow on the scale of the

169   corresponding correlation time $t_c \sim l_c^2/D$ (Fieremans et al., 2010). In other words, KM

170   is an *effective theory* valid at long times $t, t_{ex} \gg t_c$ and small wave vectors $q \ll 1/l_c$,

171   at which point the assumptions of Gaussian diffusion and exchange occurring at every

172   point in space can become justified, and ordinary rate equations can be used instead

173   of solving a genuine partial differential equation for the diffusion in a complex tissue

174   geometry.

175

176   Compartment anisotropy, essential for neuronal tissue, can be further incorporated

177   into KM (understood as an effective theory), using the steps analogous to building the
9

Correspondence to Hong-Hsi Lee

178   Standard Model. First, exchange within a perfectly aligned fiber bundle (fascicle) of

179   neurites and their extra-neurite (extracellular) space is added (assuming $t, t_{ex} \gg t_c$),

180   yielding the *anisotropic Kärger model* for aligned fibers (Fieremans et al., 2010). Next,

181   as in the Standard Model, the response of such an elementary bundle is convolved

182   with an arbitrary fiber ODF, leading to the Neurite Exchange Imaging (NEXI) (Jelescu

183   et al., 2022) and Standard Model with Exchange (SMEX) (Olesen et al., 2022) models

184   suggested recently for gray matter, where the parameter constraint of isotropic extra-

185   neurite space is further employed for the estimation robustness. We can thereby refer

186   to NEXI/SMEX as the implementations of a *locally anisotropic* (or microscopically

187   anisotropic) Kärger model, even if the overall signal from gray matter can be fairly

188   isotropic due to an almost isotropic ODF.

189

190   Fitting such anisotropic extensions of the Kärger model, or its cumulants such as the

191   time-dependent kurtosis (Fieremans et al., 2010), to the diffusion signals measured at

192   multiple diffusion times enables the quantification of exchange time scales (Jelescu et

193   al., 2022; Lee et al., 2020; Olesen et al., 2022). A prominent indicator showing the

194   dominance of the exchange phenomenon is the relative decrease in the direction-

195   averaged (spherical mean) signal as diffusion time increases for the same diffusion

196   weighting, a pattern observed in recent investigations focusing on the gray matter of

197   the mouse (Jelescu et al., 2022; Olesen et al., 2022) and human brain (Lee et al.,

198   2022; Uhl et al., 2024) and in stoke (Lampinen et al., 2021; Lätt et al., 2009). The main

199   advantage of the Kärger model is its straightforward implementation using the

200   conventional pulsed-gradient dMRI sequence, despite the demands on gradient

201   hardware to detect fast exchange effects (Williamson et al., 2023, 2019) at short

202   diffusion times. To facilitate efficient model fitting for exchange time evaluation, the

10

Correspondence to Hong-Hsi Lee

203 narrow pulse approximation has been used to derive the analytical solution of the

204 anisotropic Kärger model (Jelescu et al., 2022), though the potential impact of this

205 approximation on exchange time measurements in clinically relevant scenarios with

206 varying signal-to-noise ratios (SNR) remains unclear. Clarifying this aspect is crucial

207 for the robust interpretation of exchange dynamics in clinical and preclinical settings.

208

209 Recent advances in MRI gradient systems present significant opportunities for *in vivo*

210 tissue microstructure imaging using dMRI (Feinberg et al., 2023; Foo et al., 2020;

211 Huang et al., 2021). The first-generation Connectome MRI scanner (Connectome 1.0;

212 C1) was equipped with a high-performance gradient system achieving a maximum

213 strength of 300 mT/m and a maximum slew rate of 200 T/m/s (Setsompop et al., 2013).

214 This system enabled *in vivo* human dMRI with enhanced diffusion weighting and

215 superior SNR compared to clinical scanners. Recent studies have demonstrated the

216 feasibility of employing such a system to probe the *in vivo* exchange time using pulsed-

217 gradient based NEXI (Uhl et al., 2024) or dMRI of free gradient waveform (Chakwizira

218 et al., 2023). Recently, a second-generation Connectome MRI scanner (Connectome

219 2.0; C2) was developed, featuring an improved high-performance gradient system

220 capable of generating the strongest gradients for head-only *in vivo* human imaging at

221 3T to date, with a maximum gradient strength of 500 mT/m and a maximum slew rate

222 of 600 T/m/s (Huang et al., 2021). These enhancements offer the potential for dMRI

223 measurements at even stronger diffusion weighting with reasonable SNR, facilitating

224 the exploration of intercompartmental exchange effects across a wider range of

225 diffusion times using the Karger models.

226

11

Correspondence to Hong-Hsi Lee

227   The increasing availability of high-performance gradient systems for *in vivo* imaging,

228   such as the Siemens Cima.X system (maximum strength of 200 mT/m, maximum slew

229   rate of 200 T/m/s, whole-body 3T), GE SIGNA MAGNUS system (Foo et al.,

230   2020) with HyperG gradients (maximum strength of 300 mT/m, maximum slew rate

231   of 750 T/m/s, head-only 3T) and high-performance gradient insert (maximum strength

232   of 200 mT/m, maximum slew rate of 600 T/m/s) (Weiger et al., 2018), provides

233   essential feasibility to study the intercompartmental exchange times on *in vivo* human

234   brain using NEXI. The primary goal of this study has been to investigate

235   intercompartmental exchange times across the living human cortex using the stronger

236   and faster gradients of the Connectome 2.0 MRI scanner compared to those estimated

237   with a protocol compatible with the Connectome 1.0-alike systems. Furthermore, we

238   sought to evaluate the impact of the narrow pulse approximation on exchange time

239   estimation. Finally, we demonstrated a novel tool leveraging GPU processing to

240   accelerate the NEXI model fitting process, thereby enhancing the efficiency and

241   scalability of parameter estimation for tissue microstructure imaging.

242

243   2. Theory

244   2.1. Anisotropic Kärger Model

245   We utilized the anisotropic Kärger model (Fieremans et al., 2010; Jelescu et al., 2022;

246   Olesen et al., 2022) to model the exchange effect between neurites and extracellular

247   water in gray matter (Figure 1a). Briefly, the anisotropic Kärger model comprises two

248   exchanging Gaussian compartments: an anisotropic "stick"-like neurite compartment

249   with zero diffusivity perpendicular to the long axis, and its local extracellular space.

12

Correspondence to Hong-Hsi Lee

250 We assumed isotropic diffusion in the extracellular space to simplify the signal model

251 and improve the robustness of estimation by reducing the number of model

252 parameters. Considering a medium composed of neurites (n) and the extracellular

253 water (e), its signal representation can be written as (Fieremans et al., 2010; Kärger,

254 1985; Ning et al., 2018):

255
$$\frac{d}{dt}\begin{bmatrix} M_n(t) \\ M_e(t) \end{bmatrix} = \left(\begin{bmatrix} -r_n & r_e \\ r_n & -r_e \end{bmatrix} - q^2(t) \begin{bmatrix} D_n \varepsilon^2 & 0 \\ 0 & D_e \end{bmatrix} \right) \begin{bmatrix} M_n(t) \\ M_e(t) \end{bmatrix} \ [Eq.\,1]$$

256 where $M_{\{n,e\}}(t)$ are the both T$_1$-weighted and T$_2$-weighted magnetizations of neurite

257 and extracellular water, respectively, at diffusion time t, $r_{\{n,e\}}$ are the exchange rates

258 from neurite to extracellular water and vice versa, such that the two compartments

259 satisfy the detailed balance $r_n f_n = r_e f_e$ with neurite volume fraction $f_n = f =$

260 $\frac{M_n(0)}{M_n(0)+M_e(0)}$ and extracellular volume fraction $f_e = 1 - f$, and $D_{\{n,e\}}$ are the along-

261 neurite and isotropic extracellular water diffusivities, respectively. Here, we assumed

262 the longitudinal and transverse relaxation times of the neurite and extracellular water

263 to be the same, and the echo time dependence due to transverse relaxation and the

264 effect of coil sensitivity are cancelled out after normalized the measurements by the

265 *b*=0 signal. The diffusion wave vector $q(t)$ represents the diffusion gradient profile

266 $G(t)$ such that $q(t) = \gamma \int_0^t G(t') \mathrm{d}t'$ with the gyromagnetic ratio γ and *b*-value $b =$

267 $\int_0^t q^2(t') \mathrm{d}t'$ defining the diffusion weighting. The directional dependence is embodied

268 in the dot product $\varepsilon = \hat{n} \cdot \hat{g}$ between the neurite orientation $\hat{n}$ and the diffusion gradient

269 direction $\hat{g}$. The exchange time between the neurite and extracellular water is defined

270 as $t_{ex} = 1/(r_n + r_e) = (1-f)/r_n$. To account for the fiber dispersion of neurites in an

271 MRI voxel, the diffusion signal $S(b, \hat{g}, t)$ can be expressed as the convolution of the

13

Correspondence to Hong-Hsi Lee

272   overall signal kernel $K(b, \varepsilon, t) = M_n + M_e$ from Eq. (1) with the ODF $\mathcal{P}(\hat{n})$ (Novikov et

273   al., 2018b):

274
$$S(b, \hat{g}, t) = \int_{|\hat{n}|=1} d\hat{n}\, \mathcal{P}(\hat{n})\, K(b, \varepsilon, t). \, [Eq.\,2]$$

275   For any linear tensor encoding gradient waveform, e.g., pulsed-gradient sequence of

276   finite pulse width (Stejskal and Tanner, 1965), the overall fiber response $K(b, \varepsilon, t)$

277   entering Eq. (2) can be calculated by numerically solving the system of coupled

278   differential equations Eq. (1). Here, we refer to this method as SMEX (Olesen et al.,

279   2022). It is worth noting that while the soma compartment is not explicitly accounted

280   for in the NEXI/SMEX model, it is considered part of the extracellular compartment by

281   assuming the soma and extracellular water have similar diffusion properties and/or

282   being well-mixed (Olesen et al., 2022). Further, the exchange between soma and

283   extracellular compartments is assumed negligible due to the small surface-to-volume

284   ratio of somas, compared with neurites. More details about the theory and

285   assumptions can be found in (Olesen et al., 2022).

286

14

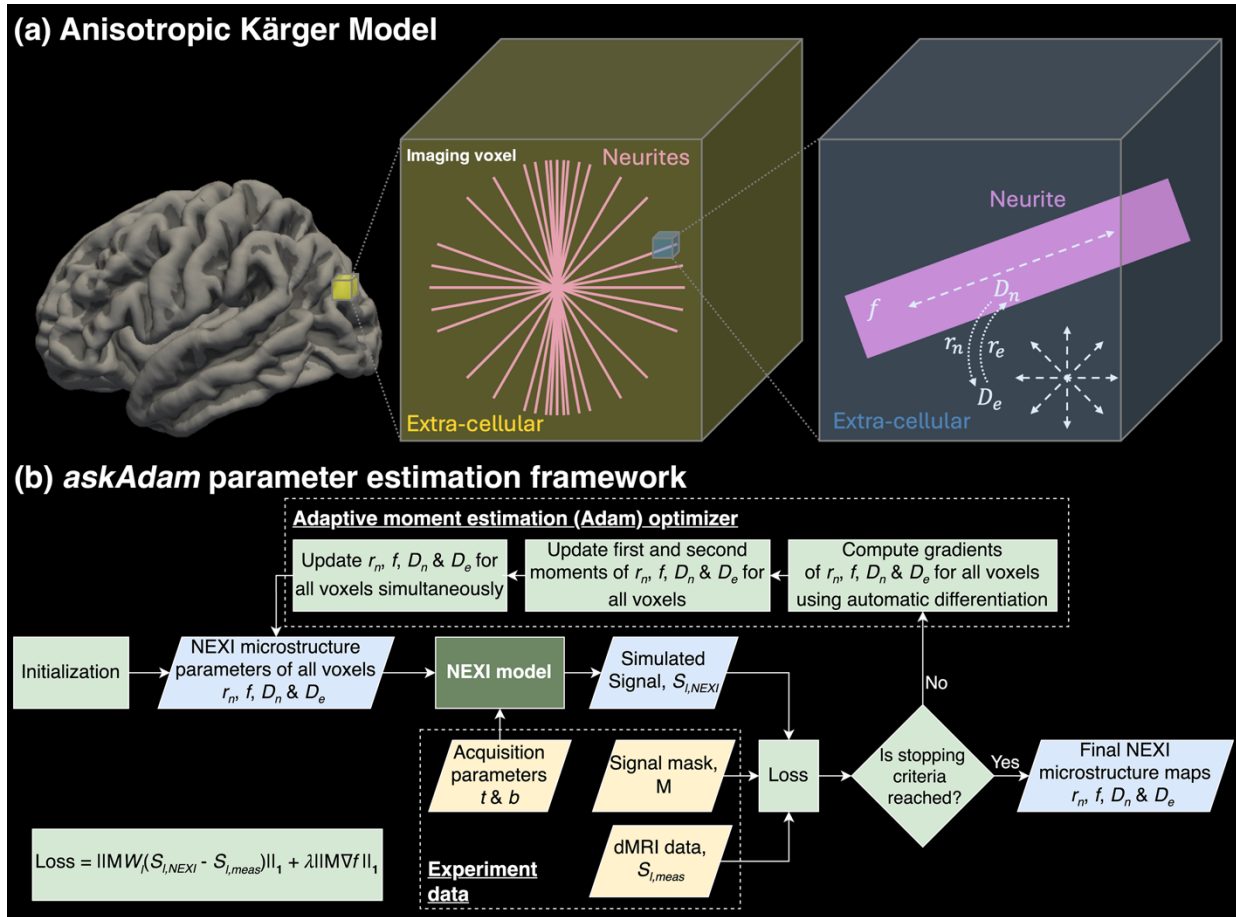Correspondence to Hong-Hsi Lee

287

288 Figure 1: (a) Graphical illustration of the anisotropic Kärger model comprising the neurite compartment
289 and extracellular water compartment. Each MRI voxel contains multiple neurites with various
290 orientations. Intercompartmental water exchange takes place between neurites and extracellular water
291 through various water movement mechanisms. (b) Illustration of the askAdam parameter estimation
292 approach used in this work.

293

294 While Eq. (1) is a general representation of the fiber bundle (fascicle) response for any

295 gradient profile, computing the dMRI signals requires solving the coupled equations in

296 Eq. (1) using numerical solvers, which is computationally costly and results in a lengthy

297 model fitting process. Alternatively, under the narrow pulse approximation, the solution

298 of Eq. (1) has an analytical form (Fieremans et al., 2010; Kärger, 1985):

299
$$K(b, \varepsilon, t) = f_1' e^{-a_1} + f_2' e^{-a_2} \ [Eq.\,3]$$

300
$$a_{1,2} = \frac{1}{2}\left(bD_n\varepsilon^2 + bD_e + tr_n + tr_e \pm \sqrt{(bD_n\varepsilon^2 - bD_e + tr_n - tr_e)^2 + 4tr_nr_e}\right) \ [Eq.\,4]$$

15

Correspondence to Hong-Hsi Lee

301
$$f'_{1,2} \equiv \pm \frac{b(fD_n\varepsilon^2 + (1-f)D_e) - a_{2,1}}{a_1 - a_2} \quad [Eq.5]$$

302 which has been referred to as NEXI (Jelescu et al., 2022).

303

304 The NEXI microstructure parameters, f, D_n, D_e and r_n, can be estimated using the

305 rotationally invariant mapping framework (Novikov et al., 2018b; Reisert et al., 2017)

306 in which both the signal model and the measured dMRI signal are projected onto the

307 spherical harmonics space after normalizing the diffusion-weighted signal by b=0

308 signal. The l-th order rotationally invariant signal S_l can be represented as:

309
$$S_l(b, t, f, D_n, D_e, r_n) = p_l K_l(b, t, f, D_n, D_e, r_n), \quad l = 0, 2, \dots \quad [Eq.6]$$

310 where the rotational invariant p_l characterizes the ODF anisotropy for each order l and

311 $p_0 \equiv 1$ (ODF normalization), and K_l is the projection of signal kernel $K(b, \varepsilon, t)$ onto the

312 Legendre polynomials. Specifically, the zeroth-order signal invariant $S_{l=0}$ corresponds

313 to the commonly known directionally averaged, spherical mean signal (Kaden et al.,

314 2016). Higher-order invariants $S_{l=2,4,\dots}$ may also contain microstructure information

315 when the ODF is anisotropic.

316

2.2. GPU-accelerated 'askAdam' framework for NEXI parameter estimation

319 Estimation of the NEXI microstructure parameters from Eqs. [3-6] involves

320 optimization on a 4-dimensional parameter space (one more additional dimension for

321 every order l from $l = 2,4,6,\dots$). Utilizing conventional nonlinear least-square

322 approaches based on CPU computation for NEXI parameter estimation can be

323 computationally lengthy for whole-brain mapping: the fitting process is repeated

16

Correspondence to Hong-Hsi Lee

324   hundreds of thousands of times sequentially over all voxels in an imaging volume.

325   Recent research has demonstrated the efficiency of accelerating the parameter

326   estimation process based on GPU computation, both on minimization based (Harms

327   et al., 2017; Hernandez-Fernandez et al., 2019) and supervised learning-based

328   approaches (Jung et al., 2021; J. Lee et al., 2019; Martins et al., 2021; Nedjati-Gilani

329   et al., 2017). Here, we incorporated NEXI parameter estimation into the 'askAdam'

330   framework (Chan et al., 2022; Marques et al., 2023), one of the minimization-based

331   GPU-accelerated methods, aiming to provide an additional resource to shorten the

332   estimation processing time while maintaining similar estimation performance to the

333   conventional CPU-based non-linear least-square (NLLS) approach.

334

335   'AskAdam' is a parameter estimation tool (Chan et al., 2022; Marques et al., 2023),

336   leveraging the efficiency and suitability of the stochastic gradient-descent-based

337   optimizer, such as Adam, to handle large non-convex problems. The Adam optimizer

338   is commonly used in deep learning to perform learnable network parameter updates

339   (Kingma and Ba, 2014) (Figure 1b). To enable askAdam to process multiple voxels at

340   the same time in NEXI parameter mapping, the optimization problem can be

341   formulated as:

342    $$\text{argmin}_{f, D_n, D_e, r_n} \left\| M W_l \left(S_{l,meas}(b,t) - S_l(b,t,f,D_n,D_e,r_n) \right) \right\|_{\text{L1/L2/MSE}} \quad [Eq.\,7]$$

343   where M is the (brain) signal mask, $W_l = 1/\sqrt{4\pi(2l+1)}$ is the weight associated with

344   the l-th order rotationally invariant signal (Novikov et al., 2018b) and $S_{l,meas}$ is the l-th

345   order rotationally invariant signal from the actual measurements. The optimization loss

346   shown in Eq. (7) is nearly identical to that used for an NLLS solver in conventional

347   voxelwise fitting. The main difference is that all input voxels inside the signal mask

17

Correspondence to Hong-Hsi Lee

348 (which can be a full set or subset of the whole-brain data, depending on the memory

349 allowance of the GPU) contribute to one loss in a single optimization problem in the

350 askAdam framework. Here, the initialization of the NEXI microstructure parameters

351 can be done by using random values or prior estimates as in NLLS. During each

352 optimization cycle, the NEXI microstructure parameters of all voxels are incorporated

353 with the sequence settings (e.g., diffusion times and b-values) to forward simulate the

354 NEXI signals across the entire volume using elementwise arithmetic operations to

355 derive the loss in Eq. (7). The loss gradient with respect to the model parameters on

356 each voxel is then computed using the automatic differentiation function from Matlab,

357 so that the model parameter across the entire dataset can be updated simultaneously

358 using the Adam optimizer (Figure 1b). All computations (i.e., forward signal generation,

359 gradient computation and parameter update) can take place on a GPU to accelerate

360 the optimization process. This process is repeated until the stopping criteria are

361 fulfilled (either the maximum number of optimization iterations is reached or the

362 change of loss across iterations is less than a certain tolerance value; a maximum of

363 4000 iterations and a tolerance level of 1×10^{-8} were chosen here). We choose the L1-

364 norm as the loss function in Eq. (7) as it outperforms the L2-norm at moderate SNR in

365 our preliminary analysis (see Figure S1).

366

367 Another advantage of askAdam is that the loss function can be further customized to

368 include spatial regularization as part of the optimization problem, which has been used

369 in image reconstruction (Knoll et al., 2011), quantitative susceptibility mapping (QSM

370 Consensus Organization Committee et al., 2024) and multi-compartment parameter

371 fitting (Orton et al., 2014; Pasternak et al., 2008) to improve the estimation results. To

372 do so, the loss function of Eq. (7) can be generalized into:

18

Correspondence to Hong-Hsi Lee

373 $$\text{argmin}_{f,D_n,D_e,r_n} \left\| MW_l \left(S_{l,meas}(b,t) - S_l(b,t,f,D_n,D_e,r_n) \right) \right\|_{\text{L1/L2/MSE}} + \lambda \mathcal{R} \quad [Eq.\,8]$$

374 where λ is a regularization parameter and $\mathcal{R}$ can be any regularizer that promotes

375 certain features (for example, sparsity or smoothness) in the estimation maps. This

376 feature is feasible for askAdam because the microstructure parameters of all voxels

377 update simultaneously during the model fitting process, in turn, allowing the regularizer

378 to stay up to date during the optimization cycle.

379

3. Methods

3.1. Numerical simulations

3.1.1 Noise propagation with forward SMEX and NEXI signal generation

383 To address the research question of whether the narrow pulse solution employed in

384 NEXI is sufficient to represent the dMRI signal in an actual experiment for high-

385 gradient performance MRI systems, we conducted a noise propagation analysis to

386 evaluate the estimation performance of the NEXI model fitting using SMEX and NEXI

387 for forward signal generation with realistic dMRI acquisition protocols designed for

388 either the Connectome 1.0 or Connectome 2.0 scanner as shown in Table 1. We

389 randomly chose 10,000 different combinations of the NEXI microstructure parameters

390 within the following range: t_{ex}=[1, 50] ms, f=[0.01, 0.99], D_n=[0.1, 3] μm²/ms, and

391 D_e=[0.1, 3] μm²/ms with $D_n \geq D_e$. Complex-valued Gaussian noise was applied to the

392 simulated signals to simulate a clinically relevant SNR of 50 in the non-diffusion-

393 weighted b=0 signal. Realistic Rician noise conditions were simulated by extracting

394 the magnitude of the signal with complex-valued Gaussian noise. NEXI model fitting

395 was subsequently performed on the spherical mean (zeroth order rotational invariant)

19

Correspondence to Hong-Hsi Lee

396   after normalized to b=0 images. The starting point of the estimation for each voxel was

397   set up using a dictionary-matching approach (Ma et al., 2013), achieved by searching

398   the maximum likelihood of the inner product of the *in vivo* measured signal to a

399   dictionary of 10,000 randomly generated simulated signal across a predefined range

400   of r_n=[0.001, 0.99] s^{-1}, f=[0.01, 0.99], D_n=[1.5, 3] μm^2/ms and D_e=[0.5, 1.5] μm^2/ms.

401   The fitting boundary of each NEXI parameter was set to: r_n=[0, 1] s^{-1}, f=[0, 1], D_n=[0.1,

402   3] μm^2/ms, D_e=[0.1, 3] μm^2/ms, and we did not impose the same constrain of $D_n \geq D_e$

403   as in the ground truth used in forward signal simulation. The forward SMEX and NEXI

404   signals were calculated for 64 diffusion gradient directions per shell. Additionally, we

405   investigated a noise-floor-correction method for the signal with Rician noise by

406   integrating the Rician noise floor within the signal model by using the Rician mean

407   model (Jelescu et al., 2022). We repeated this process based on the Connectome 2.0

408   protocol with varying diffusion gradient pulse duration $\delta = 8$ ms and 10 ms,

409   respectively, to consider its impact on Connectome 1.0-alike systems with a relatively

410   lower maximum gradient amplitude and slower gradient slew rate.

411

412   **3.1.2. Noise propagation with $l_{max} = 0$ and $l_{max} = 2$ NEXI models**

413   As introduced in the Theory section, NEXI model fitting is not limited to the spherical

414   mean signal (zeroth order rotational invariant), but can involve any spherical

415   harmonics order up to l_{max}, depending on the total number of unique gradient

416   directions acquired for each b-value. In the second noise propagation analysis, we

417   investigated if the estimation performance could be improved when the second-order

418   rotational invariants of the dMRI signals were added to the model fitting. From now on,

419   we refer to fitting the zeroth order rotational invariant $S_{l=0}$ of NEXI as $l_{max} = 0$, and to

20

Correspondence to Hong-Hsi Lee

420   fitting both invariants ($S_{l=0} + S_{l=2}$) of NEXI as $l_{max} = 2$. Noise propagation was

421   conducted under the same conditions as in Section 3.1.1, and the range of the non-

422   linear neurite dispersion index p_2 was within [0, 0.3] for the forward simulations. The

423   p_2 value increases with the tissue anisotropy (Novikov et al., 2018b). The low p_2 value

424   in simulations was consistent with the low anisotropy observed in gray matter.

425

426   Table 1: Data acquisition protocols for dMRI in this study. The same protocol parameters are used in

427   the noise propagation analysis and *in vivo* imaging. Diffusion gradient duration is defined as the full

428   width at half maximum of the gradient pulse. The maximum ramp time of the gradient pulse was

429   (500/600=)0.83 ms for the Connectome 2.0 protocol and (300/200=)1.5 ms for the Connectome 1.0

430   protocol. For each diffusion time, the gradient strength was the only control variable to achieve various

431   b-values, and the highest b-value utilized the maximum gradient strength of 300 mT/m on the

432   Connectome 1.0 protocol and 500 mT/m on the Connectome 2.0 protocol. *b=1 ms/µm² data was not

433   used in data fitting.

Protocol	Connectome 2.0			Connectome 1.0		
Diffusion time t (ms)	13	21	30	21	30	40
Diffusion gradient duration δ (ms)	6			10		
# gradient directions per shell	32 (for C1 vs C2 comparison)/64 (for high SNR cortical investigation)			32		
# shells	5	6	7	5	6	7
b-values (ms/µm²)	[1*,2.3,3.5,4.8,6.5]	[1*,2.3,3.5,4.8,6.5,11.5]	[1*,2.3,3.5,4.8,6.5,11.5,17.5]	[1*,2.3,3.5,4.8,6.5]	[1*,2.3,3.5,4.8,6.5,11.5]	[1*,2.3,3.5,4.8,6.5,11.5,17.5]
T_{acq} (min)	21	25	29.5	24	29	34

434

21

Correspondence to Hong-Hsi Lee

3.1.3. Comparison between NLLS and askAdam on NEXI parameter mapping

The askAdam framework allows data fitting to be performed simultaneously in multiple spatial dimensions with the option to incorporate spatial regularization, which is distinct from voxel-wise NLLS fitting. Therefore, we wanted to understand how this spatial regularization would affect the estimation performance between the two solvers via an *in silico* head phantom experiment. The phantom was created using the *in vivo* NEXI fitting results of one participant scanned with the Connectome 2.0 scanner (see details in Section 3.2.4). The median value across each brain parcellation label (excluded ventricles and cerebrospinal fluid) was computed for all NEXI microstructure parameters and used as the ground truth for the corresponding region of interest (ROI) segmented using FreeSurfer (Section 3.2.2). We then forward simulated the NEXI signals using the Connectome 2.0 dMRI acquisition protocol in Table 1. Gaussian noise was added to the simulated signals so that we could investigate the estimation performance at a moderate SNR of 50 and a low SNR of 25. Tissue microstructure parametric maps were derived using the NEXI $l_{max} = 2$ model implementation via either NLLS or askAdam solvers. Additionally, we incorporated anisotropic, two-dimensional spatial total variation (TV) regularization on the neurite fraction map for the NEXI model fitting with askAdam (askAdam$_{TV}$). This was achieved by applying a 2D gradient operator ($\nabla = [\nabla_x; \nabla_y]$) on the f map in the in-plane direction, i.e., $\mathcal{R} = \|M\nabla f\|_1$ in Eq. (8) (Figure 1b). The regularization parameter λ is empirically set to 0.002 mm (see Supplementary Figure S2 for details). We evaluated the accuracy of estimation via the median differences (bias) between the estimated values and ground truth, and the precision via the interquartile range (IQR) of the fitted values within each ROI. For all data fitting, the NLLS approach was performed on an EPYC 7313 16-Core

22

Correspondence to Hong-Hsi Lee

459   Processor (AMD, Santa Clara, US), whereas the askAdam approach was performed

460   on an A40 GPU (NVIDIA, Santa Clara, US).

461

462   ## 3.2. *In vivo* MRI

463   ### 3.2.1 Data Acquisition

464   **Comparison between Connectome 1.0 and Connectome 2.0 protocols**

465   Data acquisition was performed on the 3T Connectome 2.0 scanner (MAGNETOM

466   Connectom.X, Siemens Healthineers, Erlangen, Germany) equipped with a maximum

467   gradient strength of 500 mT/m and slew rate up to 600 T/m/s. Imaging experiments

468   were performed on 5 healthy volunteers (mean±SD age = 26±6 years; 3 females, 2

469   males) using a custom-built 72-channel head coil for signal reception (Mahmutovic et

470   al., 2024). The study was approved by the local ethics committee, and written informed

471   consent was obtained from all participants for being included in the study. The imaging

472   protocol comprised:

473   (1) Whole-brain T_1-weighted scan using MPRAGE with 0.9 mm isotropic resolution,

474   acquisition time = 5.5 min;

475   (2) 2D spin-echo EPI-dMRI, multi-band factor of 2, GRAPPA factor of 2, partial

476   Fourier of 6/8, resolution = 2 mm isotropic, $TR/TE_{C1}/TE_{C2}$ = 3600/68/54 ms

477   using the diffusion scheme laid out in Table 1. Non-diffusion-weighted images

478   (b=0) were acquired interspersed for every 16 diffusion-weighted images

479   (DWIs). Total acquisition time = 40 min per protocol.

480

481   **NEXI measurements with higher SNR data**

23

Correspondence to Hong-Hsi Lee

482 Additionally, 10 healthy volunteers (mean±SD age = 31±15 years; 6 females, 4 males)

483 were scanned using the same hardware and imaging sequences to measure the

484 NEXI's exchange time with higher SNR data. The same C2 protocol as described in

485 Table 1 was used for this dataset, with the only modification being that 64 diffusion

486 encoding directions were acquired for each b-value instead of 32. The total acquisition

487 time is 80 min.

488

489 ## 3.2.2. Data processing

490 The MPRAGE images were processed using FreeSurfer's *'recon-all'* function for

491 cortical surface reconstruction (Fischl, 2012) and SynthSeg (Billot et al., 2023) for gray

492 matter parcellation. Diffusion MRI data were processed based on a modified

493 DESIGNER pipeline (Ades-Aron et al., 2018), including Rician-noise-floor-corrected

494 Marchenko-Pastur Principal Component Analysis (MP-PCA) image denoising with 3

495 iterations (Tournier et al., 2023; Veraart et al., 2016), Gibbs ringing artifact removal on

496 non-diffusion-weighted images based on local sub-voxel-shifts in MRtrix (Kellner et al.,

497 2016; Tournier et al., 2019), susceptibility-induced image distortion using FSL's *topup*

498 (Andersson et al., 2003), eddy current-induced distortion using FSL's *eddy* (Andersson

499 and Sotiropoulos, 2016), and gradient non-linearity distortion correction with in-house

500 code (Fan et al., 2016; Jovicich et al., 2006). Image registration between MPRAGE

501 and dMRI data was performed based on non-linear registration using ANTs (Avants

502 et al., 2011). The transformation matrices and warp fields were subsequently used to

503 transform MPRAGE-derived gray matter parcellation labels to dMRI space for

504 statistical analysis and dMRI-derived parameter maps to MPRAGE space for

505 visualization.

24

Correspondence to Hong-Hsi Lee

506

3.2.3. Investigating time dependence via ROI fitting

508 We evaluated the time dependence of the *in vivo* dMRI signals in various areas of the

509 gray matter on ROI-averaged diffusion signals. Six ROIs, including the amygdala,

510 hippocampus, frontal, parietal, temporal and occipital gray matter, were created by

511 combining the parcellation labels from SynthSeg according to (Klein and Tourville,

512 2012). Zeroth and second-order rotationally invariant dMRI signals ($S_{l=0}$ and $S_{l=2}$) on

513 each voxel were derived by projecting the directionally dependent dMRI signal up to

514 the fourth-order spherical harmonic after normalizing the DWIs by the mean *b*=0

515 images ($S_{l=4}$ was not used). The rotationally invariant signals were then averaged over

516 each ROI and across all subjects. The averaged signals were fitted to both zeroth and

517 second order ($l_{max} = 2$) spherical harmonic of the NEXI model using the NLLS

518 implementation. All diffusion times and *b*-values were used in the model fitting except

519 data acquired at *b*=1 ms/µm^2 since the restricted diffusion inside the soma

520 compartment could still have non-negligible contributions to the dMRI signal at low *b*-

521 values (see Supplementary Figure S6).

522

3.2.4. NEXI microstructure parameter mapping

524 Tissue microstructure parametric maps were derived using the NEXI $l_{max} = 2$ model

525 implementation on the whole-brain data for individual subjects via either the NLLS or

526 askAdam solvers similar to the *in silico* head phantom experiment in Section 3.1.3.

527 Additionally, we incorporated 2D-TV regularization for the NEXI model fitting with

528 askAdam to validate the *in silico* experiment findings with the *in vivo* data.

25

Correspondence to Hong-Hsi Lee

529   Subsequently, the exchange time maps were transformed into FreeSurfer's fsaverage

530   subject space and projected onto the cortical surface for visualization.

531

3.2.5. Statistical analysis

533   In subsequent statistical analyses on the whole-brain parameter maps, the median

534   value within each cortical ROI was computed to minimize outliers due to potential

535   partial volume effects and imperfect cortical surface registration between the

536   MPRAGE and dMRI images for all the NEXI microstructure parameters on each

537   subject. Group-level statistics were derived by computing the mean exchange time

538   and its standard deviation (SD) across subjects for each ROI. With the 2 mm isotropic

539   resolution of the *in vivo* data, the partial volume effect originating from the

540   cerebrospinal fluid (CSF) and superficial white matter may affect the accuracy of the

541   estimated gray matter exchange time. Therefore, we performed a Pearson's

542   correlation analysis to investigate whether the exchange time derived from NEXI was

543   associated with the cortical thickness estimated from the SynthSeg parcellation result

544   on all ROIs. Additionally, we computed the Pearson's correlation coefficients between

545   the NEXI microstructure parameters to understand how they interacted with one

546   another.

547

26

Correspondence to Hong-Hsi Lee

4. Results

4.1. Noise propagation analysis

Noise propagation results from fitting the zeroth order rotational invariant of NEXI to either SMEX or NEXI for forward signal generation showed similar estimation performance on all parameters at an SNR of 50 based on Connectome 2.0 dMRI acquisition protocol (Figure 2a). Similar observations can be made when the gradient pulse duration was set to 8 ms and 10 ms (Figure 2b). We compared the three noise correction scenarios: Rician uncorrected noise (RUC), Rician mean model (RM), and Gaussian noise. Among the three cases, the uncorrected Rician noise signal had the worst performance with greater biases and wider IQRs for all parameters (Figure 2c). Incorporating the Rician mean into the NEXI signal model (RM) or with the Gaussian noise greatly reduces the estimation biases and IQRs for all fitted parameters. Notably, the exchange time estimation from the Connectome 1.0 protocol is less accurate and less precise than those derived from Connectome 2.0 at faster exchange times ($\leq$20 ms) in the presence of the Rician noise floor. In the relatively slower exchange time regime (>20 ms), the estimation performance between the C1 and C2 is comparable in all cases (left panel, Figure 2c). Comparable noise performance was observed when using only the zeroth order rotational invariant of the signal and incorporating the second order rotational invariant into the NEXI model fitting, for all estimated parameters (Figure 2d). The noise propagation analysis result shows that the additional fitting parameter p_2 (corresponding to the nonlinear fiber dispersion index) can be robustly measured without degrading the estimation performance of the other parameters (Figure 2d).

27

Correspondence to Hong-Hsi Lee
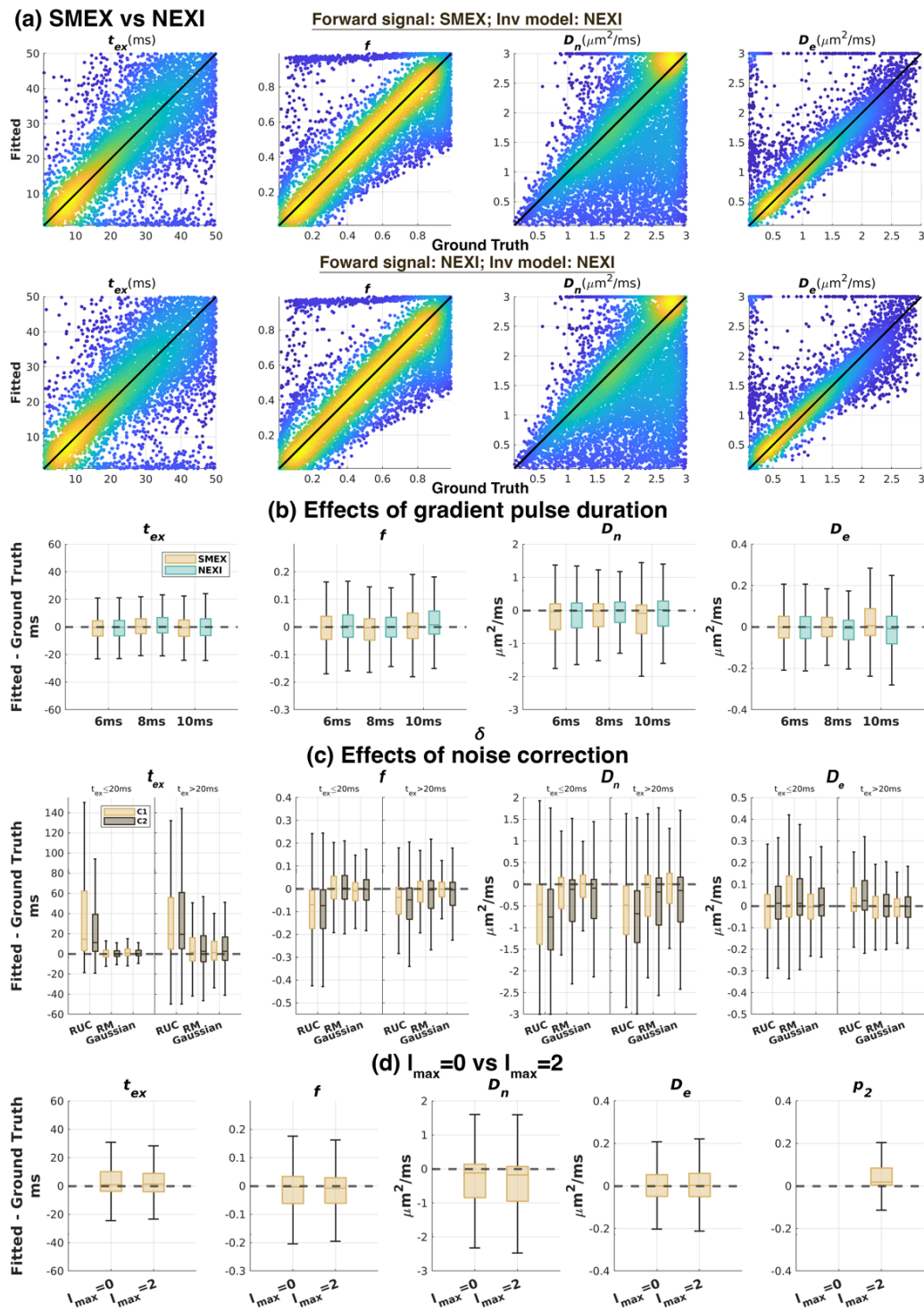
Figure 2: Noise propagation analysis evaluating the effect of the narrow pulse approximation for NEXI at SNR of 50. (a) Scatter plots of the estimated NEXI microstructure parameters versus ground truth values on data with Gaussian noise using Connectome 2.0 protocol. Color scale corresponds to the occurrence on the spatial grid (Yellow: high occurrence; Blue: low occurrence). (b) Box plots of the NEXI parameters estimated with various gradient pulse durations. (c) Box plots of the NEXI parameters estimated with various Rician noise floor correction methods. (d) Box plots of the NEXI parameters estimated with $I_{max}=0$ and $I_{max}=2$.

28

Correspondence to Hong-Hsi Lee

580

4.2. NLLS vs askAdam

582   To determine if askAdam can be an effective optimization tool for NEXI model fitting,

583   we compared its estimation performance to the standard NLLS approach based on

584   the summary statistics across ROIs using image-based numerical simulations. The

585   processing time on the simulated whole-brain dataset phantom for the NLLS approach

586   was about 13 hours on 1 CPU, whereas the askAdam-based approaches took about

587   6 min, achieving over 100-fold acceleration on processing time by GPU. In terms of

588   accuracy and precision, we observed that askAdam was slightly less accurate than

589   NLLS for the exchange time estimation (median bias of NLLS=0.26 ms vs

590   askAdam=0.67 ms at SNR=50; Figure 3b-c), while the precision is comparable

591   (median IQR of NLLS=3.01 ms vs askAdam=3.24 ms, Figure 3d). Interestingly, the

592   measurement accuracy remains comparable with precision being improved when we

593   introduced a weak spatial regularization with askAdam in NEXI model fitting (median

594   bias of askAdam=0.67 ms vs askAdam$_{TV}$=0.56 ms; median IQR of askAdam=3.24 ms

595   vs askAdam$_{TV}$=2.64 ms at SNR=50). As SNR decreases, both the accuracy and

596   precision of the estimation are reduced for all solvers (Figure 3c-d).

597

29

Correspondence to Hong-Hsi Lee
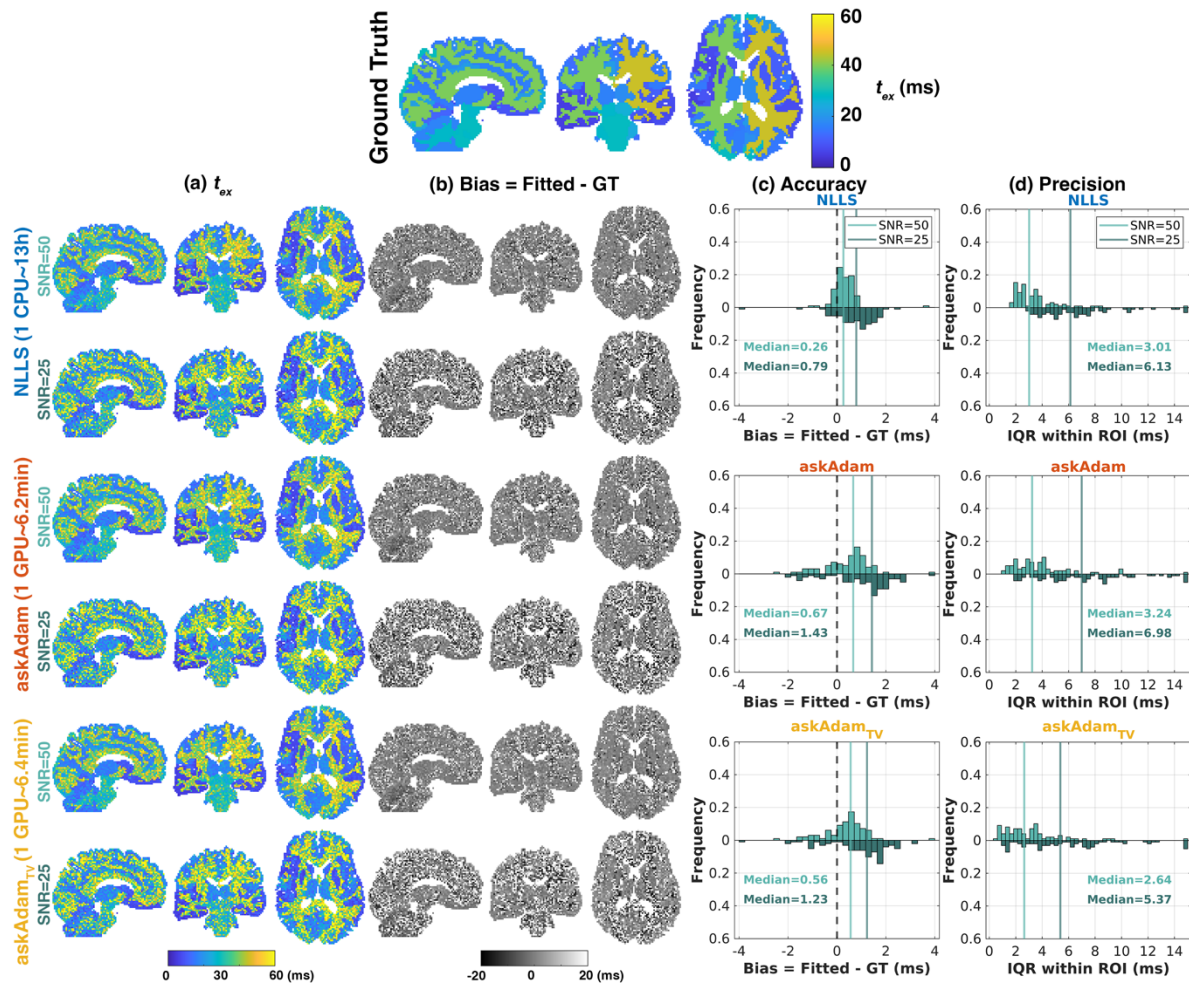
Figure 3: *In silico* head phantom comparison between NLLS and askAdam for NEXI parameter estimation performance. (a) The intercompartmental exchange time maps and (b) the corresponding estimation bias derived at SNR of 50 and SNR of 25 for the three solers: voxel-wise NLLS, askAdam without spatial regularization and askAdam with spatial regularization. (c) Estimation accuracy and (d) precision across all ROIs.

4.3. *In vivo* results

We evaluated the goodness of fit between the NEXI model fitting and the *in vivo* data using the ROI-averaged rotationally invariant signals. Time-dependent dMRI signals were observed for all gray matter ROIs (circles in Figure 4) on both Connectome 2.0 (Figure 4a) and Connectome 1.0 (Figure 4b) protocol data, where both the zeroth and second-order rotational invariants $S_{l=0}$ and $S_{l=2}$ decreased with diffusion time at each

30

Correspondence to Hong-Hsi Lee

611   *b*-value. In terms of fit quality, the discrepancies between the fitted signal curves and

612   the actual data were more noticeable on the second-order rotational invariants $S_{l=2}$,

613   with the amygdala showing the poorest fit in both cases, though the root mean square

614   values of the fitting residual are comparable between $S_{l=0}$ and $S_{l=2}$, ranging from

615   2.26×10^{-3} to 3.12×10^{-3} for $S_{l=0}$ and from 0.25×10^{-3} to 1.41×10^{-3} for $S_{l=2}$ across ROIs.

616   In this analysis, the estimated t_{ex} ranged from 14.93 ms (frontal) to 33.51 ms (occipital)

617   on the Connectome 2.0 data (Table 2), whereas the estimated t_{ex} from Connectome

618   1.0 was substantially longer when compared to Connectome 2.0, though similar

619   regional trends could be observed (faster exchange in the frontal, parietal and

620   temporal gray matter).

621

622   Table 2: Ordinary NEXI microstructure parameters of gray matter ROI derived from ROI-averaged *in*
623   *vivo* dMRI signals. C2: Connectome 2.0 protocol; C1: Connectome 1.0 protocol.

	t_{ex} (ms)		f		D_n (μm^2/ms)		D_e (μm^2/ms)		p_2	
	C2	C1	C2	C1	C2	C1	C2	C1	C2	C1
Frontal	14.93	30.22	0.35	0.27	3.00	3.00	0.89	0.90	0.21	0.24
Parietal	17.84	32.15	0.32	0.27	3.00	3.00	0.94	0.95	0.21	0.23
Temporal	17.06	39.39	0.35	0.28	3.00	3.00	0.81	0.81	0.20	0.23
Occipital	33.51	77.64	0.34	0.30	3.00	3.00	0.89	0.88	0.19	0.21
Amygdala	22.96	605.48	0.37	0.27	3.00	3.00	0.77	0.79	0.28	0.33
Hippocampus	29.36	323.18	0.36	0.28	3.00	3.00	0.82	0.83	0.28	0.32

624
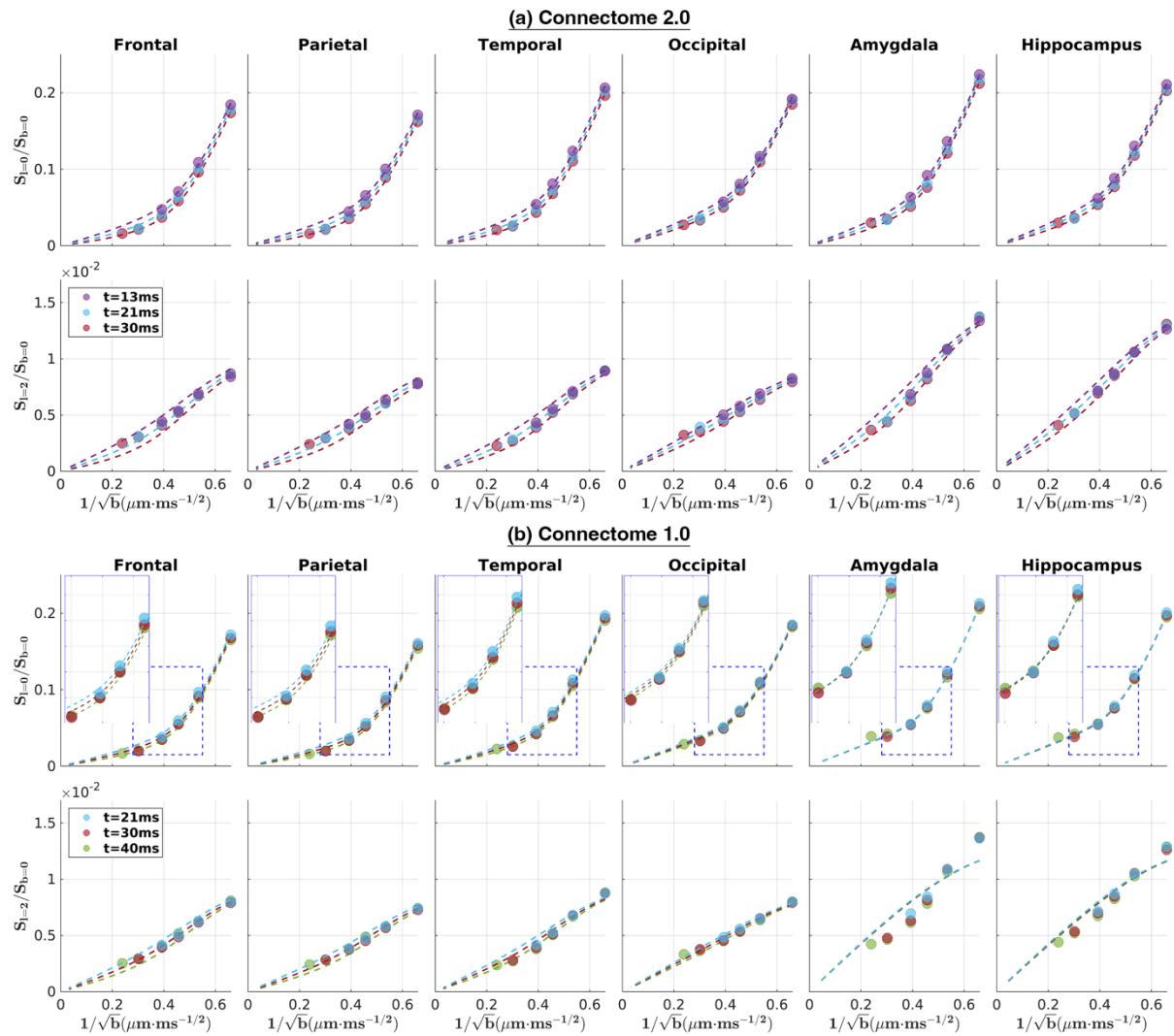
31

Correspondence to Hong-Hsi Lee

Figure 4: Results of ordinary NEXI model fitting on ROI-averaged *in vivo* dMRI signals. The NEXI model of $l_{max} = 2$ was fitted to data using the (a) Connectome 2.0, and (b) Connectome 1.0 protocol data. Circles represent the measured data and dashed lines represent the NEXI model fitting curves derived from the estimated tissue parameters.

The *in vivo* whole-brain mapping estimation differences between the Connectome 2.0 and Connectome 1.0 protocols show similar patterns as fitting the ROI-averaged signal. The estimated t_{ex} with the Connectome 1.0 protocol was about 2.67 times longer than those with the Connectome 2.0 protocol when fitting the ordinary NEXI model to the denoise dMRI data (Figure 5). Interestingly, the bias between the two protocols was reduced to a factor of 1.54 using the NEXI Rician mean model with no

32

Correspondence to Hong-Hsi Lee

637 denoising applied to the dMRI data. For the Connectome 1.0 protocol, the t_{ex}

638 estimation of using NEXI Rician mean model was substantially shorter than those of

639 using the ordinary NEXI model, while the t_{ex} estimations of the Connectome 2.0

640 protocol are comparable between the two approaches.

641
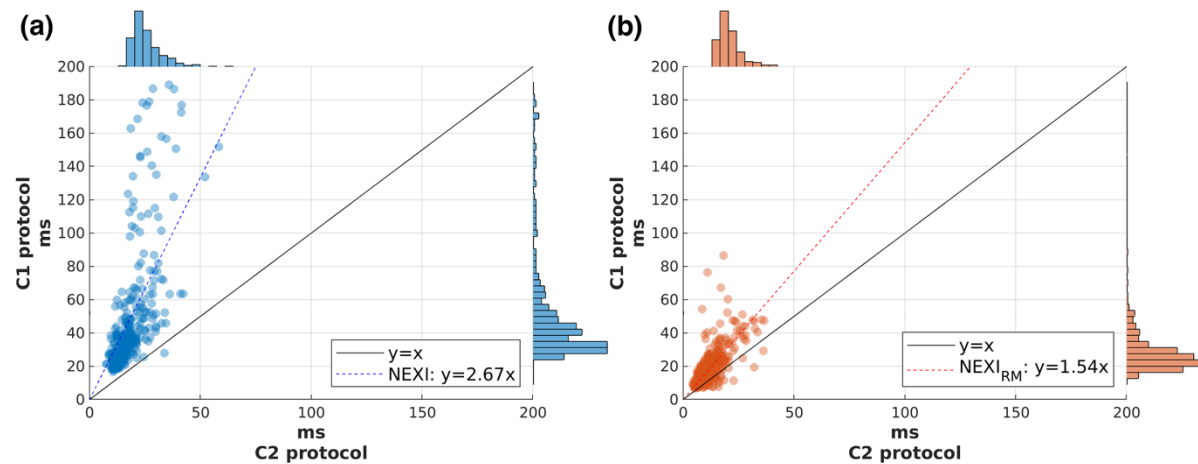
642 Figure 5: Scatterplots of the estimated exchange time using C1 and C2 protocols with (a) the ordinary
643 NEXI model with denoise dMRI data and (b) the NEXI with Rician mean model with dMRI data that did
644 not incorporate denoising in the preprocessing. Each data point corresponds to the median value of an
645 ROI.

646

647 Images of both the zeroth order and second order rotational invariants of the dMRI

648 signal demonstrated that the Connectome 2.0 scanner produced very high-quality data

649 even at high b-values (Figure 6a). The mean SNR across all subjects in the cortex

650 was 55 at b=0 without data denoising. The SNR of the spherical mean signal (spherical

651 mean signal divided by the noise estimation from b=0 images) at t=30 ms for each b-

652 values from 2.3 ms/μm^2 to 17.5 ms/μm^2 were 9.6, 5.4, 3.4, 2.4, 1.7 and 1.5,

653 respectively. These levels can be interpreted as the ratio of spherical mean signal to

654 the noise floor for each b-shell. On top of that, the noise fluctuation in spherical mean

655 signal was even smaller by a factor of $\sqrt{N}$ with N = 64 gradient directions per b-shell.

656 The *in vivo* NEXI parameter maps on a single subject are shown in Figure 6b. Among

33

Correspondence to Hong-Hsi Lee

657   all NEXI parameters, the intra-neurite diffusivity D_n was the noisiest measurement.

658   The estimated values were very close to the upper bound of the parameter range (3

659   μm^2/ms), especially in white matter, whereas the estimations of neurite volume fraction

660   f and ODF p_2 were the most robust. All three optimization solvers (NLLS, askAdam

661   and askAdam$_{TV}$) produced similar contrast on all parameters except D_n, where the

662   values from askAdam were lower than those from NLLS and close to 2.5 μm^2/ms.

663

664   The exchange time maps projected onto the cortical surface of two subjects (Subject

665   #1: 23-year-old female; Subject #2: 22-year-old male) are shown in Figure 7. In both

666   cases, the t_{ex} maps derived from NLLS were apparently noisier than those from

667   askAdam, and the results were comparable between with and without spatial

668   regularization for askAdam. In these two examples, both subjects showed similar

669   spatial contrasts between the pre-/post-central gyri, visual cortex, and cingulate gyrus

670   to their surrounding tissue.

34

Correspondence to Hong-Hsi Lee
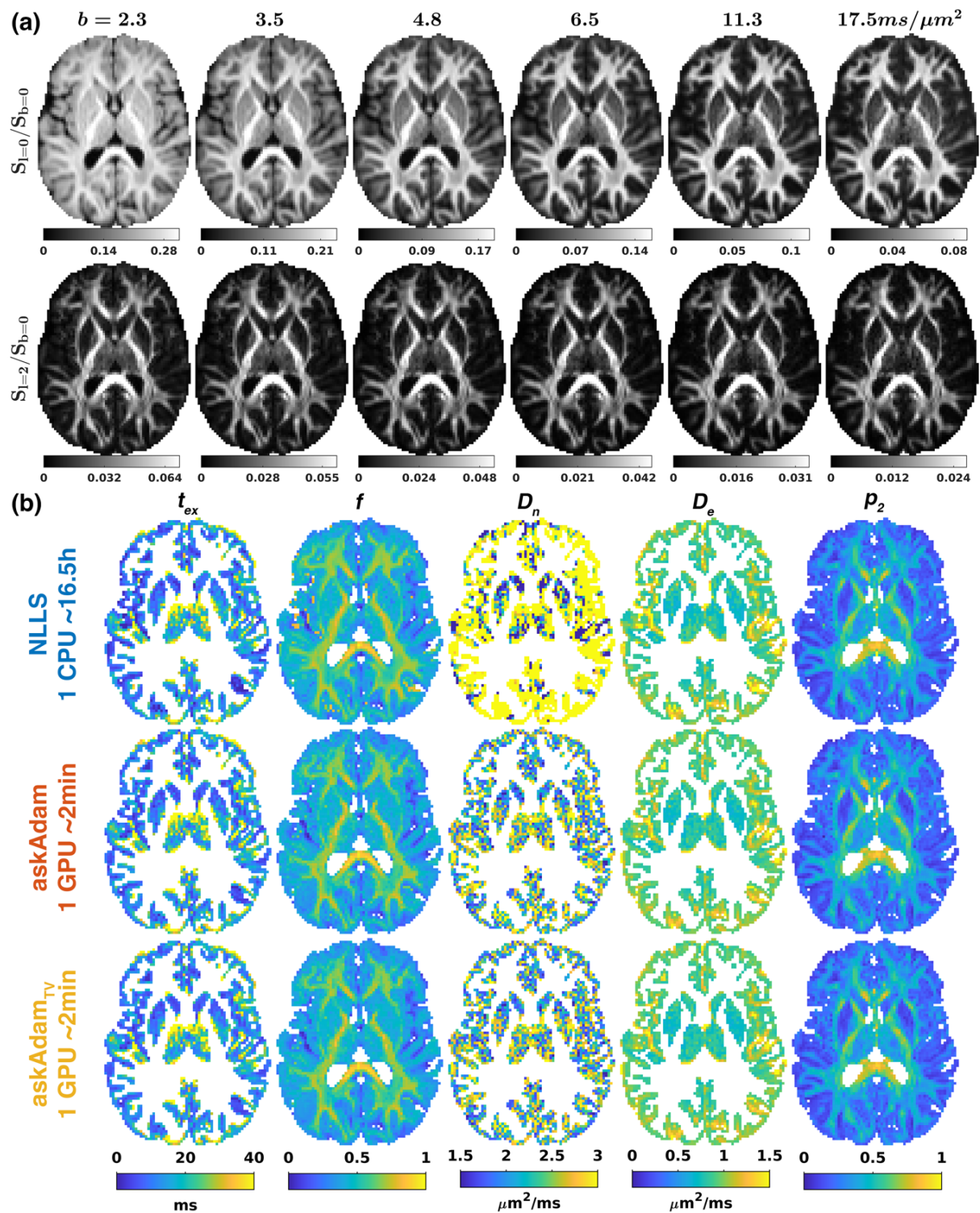
Figure 6: (a) Examples of the zeroth and second order rotationally invariant dMRI signals at t=30 ms and b-values=2.3-17.5 ms/µm^2 on one subject from the high SNR Connectome 2.0 cohort. Zoom-in images can be found in Supplementary Figure S8. (b) NEXI microstructure parameters on the same subject derived from different solvers. CSF (f and p_2) and white matter (t_{ex}, D_n and D_e) were masked out to provide a better illustration of the estimations on gray matter.
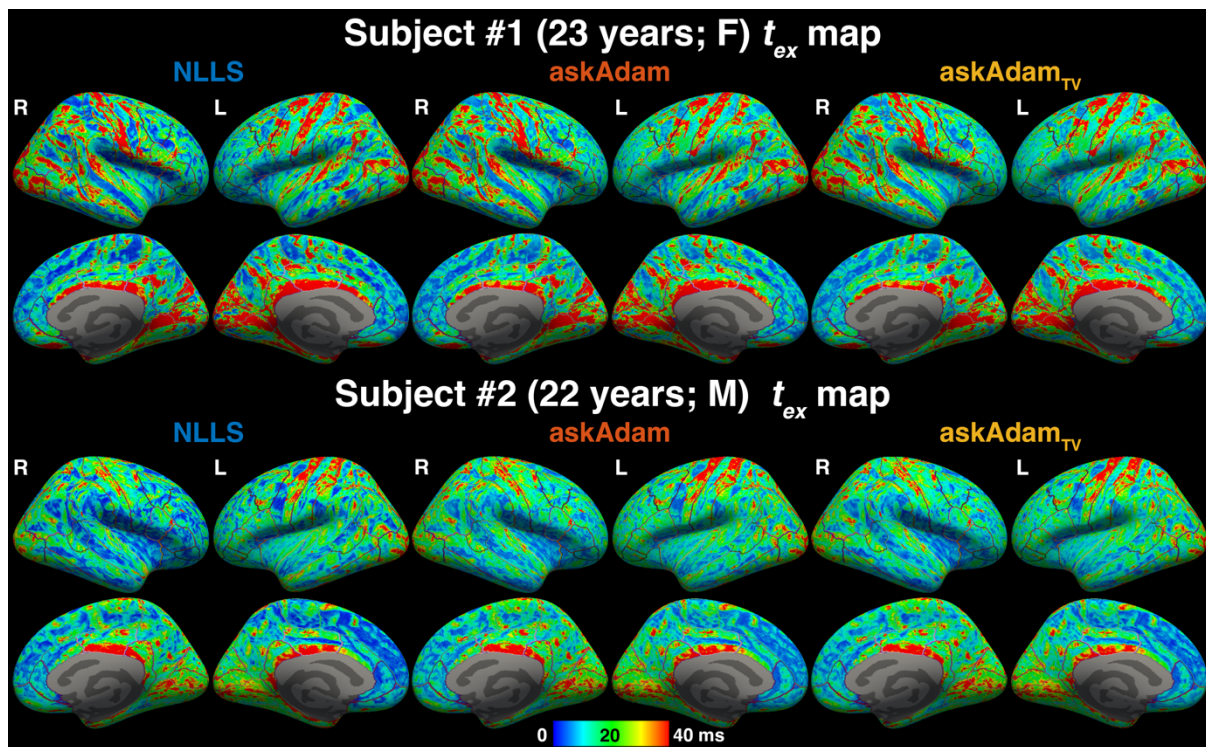
35

Correspondence to Hong-Hsi Lee

Figure 7: Examples of exchange time t_{ex} maps projected at middle cortical depth, halfway between the pial surface and gray-white matter interface in two subjects (Subject #1: 23 years; female; Subject #2: 22 years; male). The outline on the cortical surface indicates the boundaries of the SynthSeg parcellation labels.

In the group-level analysis, the median±IQR exchange times estimated using NLLS, askAdam, and askAdam$_{TV}$ were 13.1±8 ms, 13.3±7 ms and 13.2±6.9 ms across all cortical ROIs for all subjects on the high SNR Connectome 2.0 data (Figure 8a). Like the spatial patterns observed at the individual level, the frontal pole, pre-/post-central gyri, visual cortex and posterior cingulate cortex had relatively longer exchange times than other ROIs on Connectome 2.0 (Figure 8b). A spatial gradient of longer exchange times was found moving from the anterior to the posterior cingulate cortex (Figure 8b-c). The mean exchange times and standard deviations across subjects were similar for all three solvers, except for the fontal pole, entorhinal, temporal pole, and

36

Correspondence to Hong-Hsi Lee

692   parahippocampal gyrus, where the NLLS solver estimated generally longer exchange

693   times and showed larger standard deviations (Figure 8c).
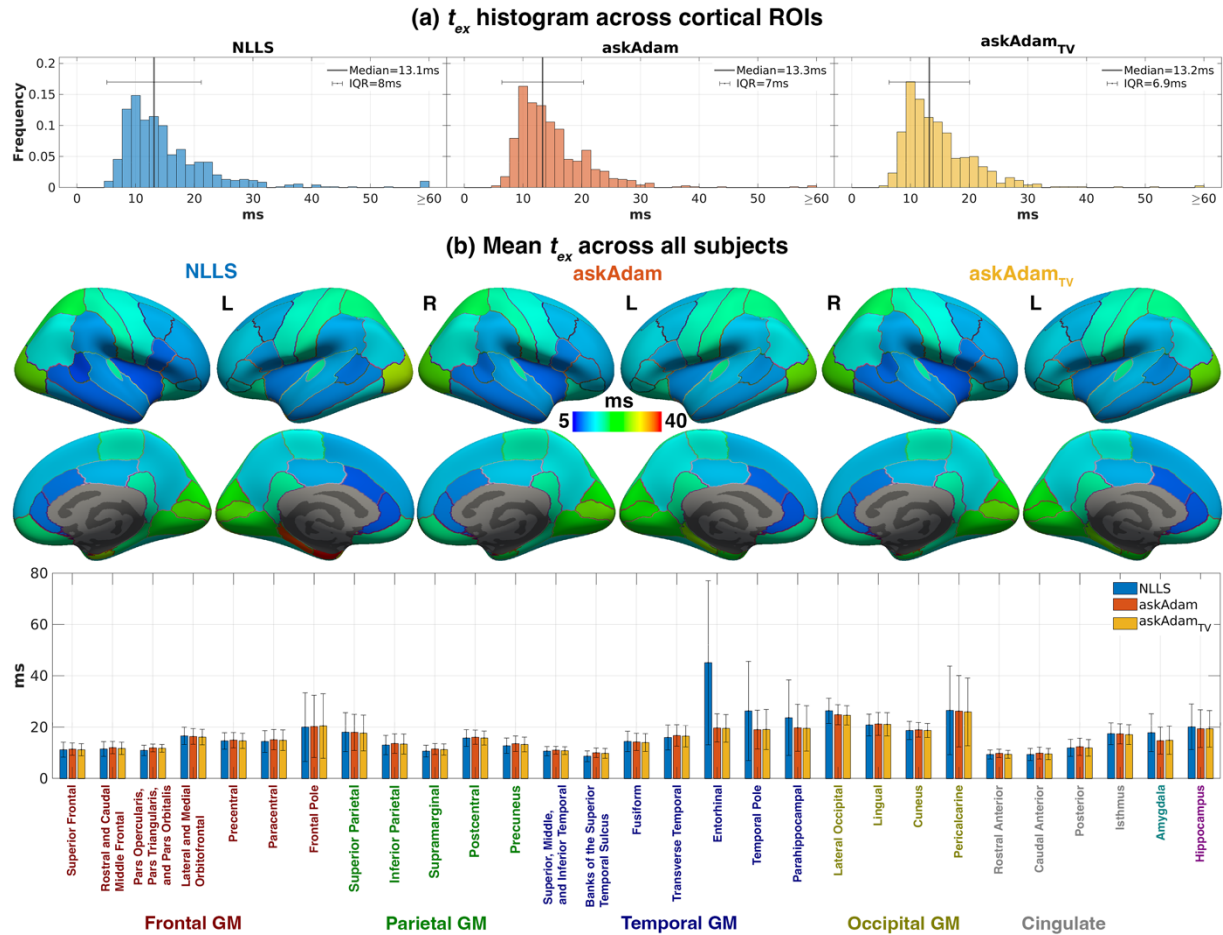
694

695

696   Figure 8: (a) Exchange time t_{ex} across all cortical ROIs and all subjects using the high SNR
697   Connectome 2.0 dataset. Solid line indicates the median exchange time of the corresponding histogram.
698   (b) Mean and standard deviation of the exchange time across all subjects for each cortical ROIs and
699   their corresponding projection on the cortical surface.

700

701   To investigate potential partial volume effects from CSF and superficial white matter

702   on NEXI model fitting, we performed a Pearson's correlation analysis between the

703   estimated exchange time and cortical thickness for all cortical ROIs and all subjects.

704   No significant correlations were found between these two parameters on all solvers

705   (R=-0.01; R=-0.02 and R=-0.02 for NLLS, askAdam, and askAdam$_{TV}$, Figure 9a).

    37

    Correspondence to Hong-Hsi Lee

706 Among the NEXI tissue parameters, moderate correlations were found between t_{ex}

707 and f (-0.48, -0.50, -0.50), between t_{ex} and D_n (-0.45, -0.43) for the askAdam solvers,

708 and between p_2 and f (-0.53, -0.34, -0.35) for NLLS, askAdam and askAdam$_{TV}$.

709 Additionally, moderate correlations were observed between p_2 and D_n (-0.37) for

710 NLLS (Figure 9b), whereas weaker correlations between these two parameters (-0.28,

711 -0.29) were observed for askAdam and askAdam$_{TV}$ (Figure 9b).

712

713
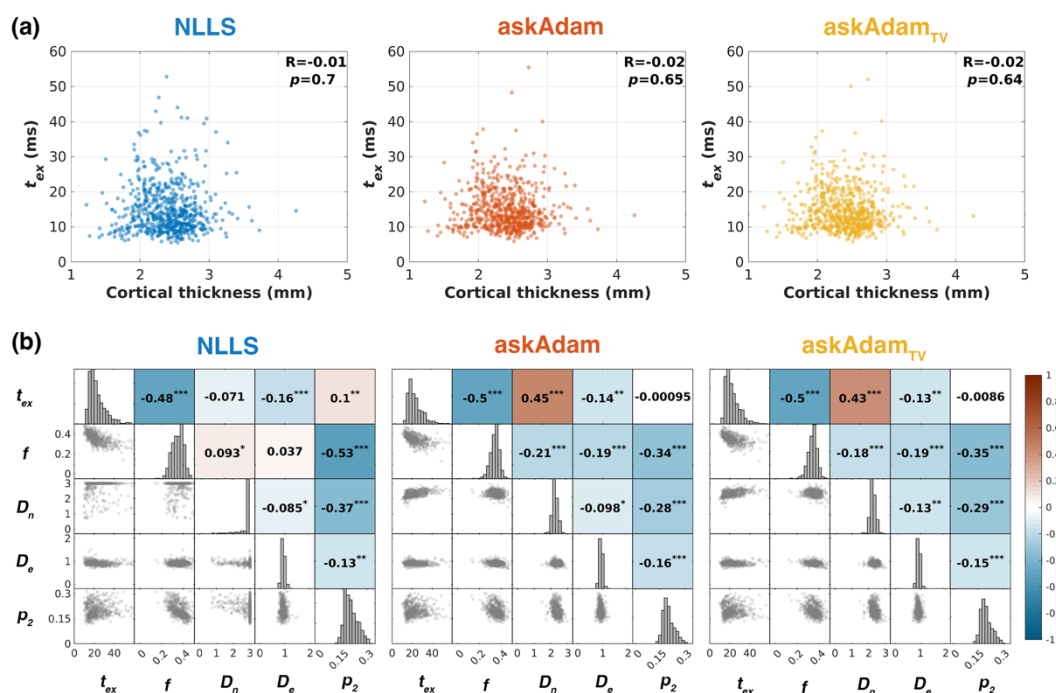
714 Figure 9: (a) Scatter plots of exchange time t_{ex} versus cortical thickness across all cortical ROIs and all
715 subjects, with Pearson's correlation coefficient R and *p*-value are also reported. (b) Correlation matrix
716 between the NEXI microstructure parameters for each solver. *p*-value<0.05; **p*-value<0.01; ***p*-
717 value<0.001.

718

5. Discussion

720 In this work, we studied the intercompartmental exchange times between neurites and

721 extracellular water in the living human brain using the NEXI model fitted to data

38

Correspondence to Hong-Hsi Lee

722   acquired on the state-of-the-art Connectome 2.0 scanner, which enabled us to obtain

723   high-quality, whole-brain dMRI data at strong diffusion weighting (*b*-values up to 17.5

724   ms/μm^2) and short diffusion time (t_{min}=13 ms). Similar to previous animal studies

725   (Jelescu et al., 2022; Olesen et al., 2022), we observed that the zeroth order rationally

726   invariant (spherical mean) dMRI signals decreased with diffusion times at each b-value

727   across the cortex, which was considered as the signature of intercompartmental

728   exchange in grey matter (Olesen et al., 2022). While the measured exchange time

729   across the human cortex using the Connectome 1.0 protocol agreed with the literature

730   with a similar setup (Uhl et al., 2024), the exchange time derived from the Connectome

731   2.0 protocol was substantially shorter, with median±IQR of approximately 13±8 ms.

732   The exchange time was observed to vary across the cortical ribbon. Furthermore, we

733   introduced a novel processing tool to accelerate NEXI model fitting by more than 100-

734   fold utilizing the latest GPU computing technology with comparable accuracy and

735   improved precision compared to conventional voxel-wise NLLS fitting.

736

737   <u>Comparison between Connectome 1.0 and Connectome 2.0 protocols</u>

738   We evaluated the inter-compartmental exchange time in the living human brain at the

739   individual level using the ultra-high-gradient performance Connectome 2.0 scanner.

740   The gradient system of the Connectome 2.0 scanner is five times more powerful than

741   its predecessor Connectome 1.0 (considering together a magnetic field gradient 1.67

742   times stronger and 3 times faster than Connectome 1.0). This allows the Connectome

743   2.0 scanner to achieve the shortest diffusion time of 13 ms instead of 21 ms as

744   Connectome 1.0 with similar diffusion weighting, facilitating access to experimental

745   conditions better suited to probing fast water exchange when the two water

746   compartments are less well mixed. Under the ideal conditions (i.e., with Gaussian

39

Correspondence to Hong-Hsi Lee

747 noise or the noise statistics considered in the signal model), our simulations suggested

748 that both Connectome 1.0 and Connectome 2.0 protocols can perform equally well

749 (Figure 2c). The advantages of the shorter diffusion times accessible on Connectome

750 2.0 are evident when the exchange time is relatively short (≤ 20 ms). Compared to the

751 Connectome 1.0 protocol, the estimation of exchange time ≤ 20 ms using the

752 Connectome 2.0 protocol was more precise and accurate, especially when the noise

753 floor was not accounted for in the signal model (left panel, Figure 2c). This observation

754 is supported by the in vivo exchange time comparison between the two protocols

755 (Figure 5), where the Connectome 1.0 derived exchange time is 2.67 times longer

756 than that of the Connectome 2.0 using the ordinary NEXI model, driven by the reduced

757 estimations in both f and r_n, whereas the Connectome 1.0 estimations using the NEXI

758 with Rician mean model became substantially shorter and more comparable to the

759 Connectome 2.0 protocol results, potentially due to the incomplete removal of the

760 noise floor by the denoising method. Note that our Connectome 1.0 *in vivo* exchange

761 times derived from the ordinary NEXI model were comparable to the results reported

762 in another study using the same method (103.9 ms using the ordinary NEXI model

763 and 42.3 ms using the NEXI with Rician mean model) (Uhl et al., 2024). Besides the

764 noise floor effect, another hypothesis that may account for the observed differences in

765 exchange times measured on Connectome 2.0 versus Connectome 1.0 could be that

766 water exchange occurs across a broad range of times, as suggested in a recent report

767 (Cai et al., 2023). As a result, using shorter diffusion times may sensitize the

768 measurement of intercompartmental water exchange to the fast exchange process.

769 Previously, shorter exchange times of 3-10 ms were observed in the *ex vivo* rat brain

770 using the SMEX model in an experiment that used relatively short diffusion times (7.5-

40

Correspondence to Hong-Hsi Lee

771   16 ms) (Olesen et al., 2022). We acknowledge that it is challenging to compare our

772   results directly with those in the *ex vivo* rat brain due to potential interspecies

773   differences in membrane permeability, tissue constituents and water transport

774   mechanisms caused by experiment conditions such as fixation and tissue preparation

775   (Williamson et al., 2023). Differences related to the dMRI acquisition protocol and

776   hardware, including the diffusion times, diffusion weightings and SNR, can also

777   introduce additional variations observed between the two studies. On the other hand,

778   Veraart et al. estimated exchange times of 10-30 ms in the *in vivo* human brain gray

779   matter using the anisotropic Kärger model (Veraart et al., 2020), and Williamson et al.

780   measured an exchange time of 10 ms in the living mouse spinal cord via two-

781   dimensional diffusion exchange spectroscopy (Williamson et al., 2023, 2019), which

782   are both in agreement with our Connectome 2.0 measurements. Other imaging factors,

783   such as SNR, may also affect the measured values. As shown in the noise propagation

784   analysis, the (residual) Rician noise floor can lead to an overestimation of the

785   exchange time (Figure 2c). Even for Gaussian noise, low SNR conditions can lead to

786   slightly overestimated exchange times as indicated by the *in silico* head phantom

787   simulations (Figure 3). Therefore, extra care may be needed on data processing and

788   result interpretation when performing NEXI on standard clinical scanners as the

789   gradient pulse duration, minimum achievable diffusion time and SNR will not be

790   comparable to high-gradient performance systems like Connectome 1.0 or 2.0.

791

792   <u>Implications on noise propagation analysis</u>

793   Our noise propagation results indicate that the narrow pulse approximation utilized in

794   the NEXI model adequately captures the exchange time given the clinically relevant

795   SNR with high gradient performance setups. This observation remains consistent
       41

       Correspondence to Hong-Hsi Lee

796   across different gradient pulse durations (6-10 ms). Although the SMEX model

797   provides a more precise representation of the exchange dMRI signals, its direct usage

798   on NLLS fitting could be relatively challenging due to the longer computational time

799   required for solving the associated ordinary differential equations, especially for whole

800   brain data. Accelerating SMEX forward signal generation using techniques such as

801   artificial neural networks may be valuable to further improve the estimation

802   performance in exchange time measurement in the future. One limitation of our

803   simulation is that we did not take the restricted diffusion from the soma compartment

804   into account for the forward signal simulation, which is also affected by the change of

805   diffusion encoding gradient duration. On the other hand, the Rician noise floor

806   correction has a more notable effect on the accuracy and precision of exchange time

807   estimation. Incorporating the Rician noise model into the NEXI signal model or having

808   Gaussian noise present in the data minimizes estimation bias, aligning with findings

809   from prior research (Uhl et al., 2024). Estimating noise levels in the data is crucial for

810   implementing the NEXI model of Rician mean, achievable through methods such as

811   MP-PCA noise level estimation (Veraart et al., 2016) or through the temporal statistics

812   on multiple b=0 images (assuming the noise level is constant over time). Alternatively,

813   techniques like Rician-bias-corrected MP-PCA denoising (Tournier et al., 2023) or

814   using real-value dMRI data (Eichner et al., 2015; Fan et al., 2020; Tian et al., 2022)

815   can reduce the Rician noise floor and potentially achieve noise statistics closer to

816   Gaussian noise conditions. However, it is of the utmost importance to ensure the noise

817   floor is eliminated by using these approaches, as the estimated exchange time is

818   highly sensitive to the residual noise floor, as illustrated in Figure 2c and Figure 5. In

819   our extended analysis, results suggest that higher-order rotational invariants of dMRI

820   signals may not contribute significantly to NEXI microstructure parameter estimation

    42

Correspondence to Hong-Hsi Lee

821 (Figure 3), likely due to the highly disperse nature of neurite orientations in gray matter.

822 In most cases, the zeroth order signals (spherical mean) are sufficient for estimating

823 the exchange time. Nevertheless, incorporating the second-order signals introduces

824 an additional microstructure parameter (p_2), representing neurite orientation

825 dispersion, without sacrificing estimation performance (see also Supplementary

826 Figure S4 and Table S1 for *in vivo* comparison), which could be relevant in disease

827 contexts.

828

829 <u>Effects of diffusion weighting on estimated exchange time</u>

830 We utilized strong diffusion weighting (maximum *b*-values of 17.5 ms/μm^2) for NEXI to

831 ensure water exchange can be sampled when the hindered diffusion of extracellular

832 water does not contribute to the diffusion signal. To gain further insight into whether

833 such strong diffusion weighting is needed to measure the exchange time accurately,

834 we performed a retrospective analysis by repeating the ROI-averaged NEXI estimation

835 using dMRI data limited to *b*=6.5 ms/μm^2. While the exchange times remain

836 comparable in frontal, parietal and occipital gray matter regions, reductions in

837 exchange time are evident in the temporal gray matter, amygdala, and hippocampus

838 when high *b*-value data are excluded (refer to Supplementary Figure S7 and Table

839 S2). This decrease in $t_{ex} = (1 - f)/r_n$ is attributed to the apparent overestimation of

840 the intra-neurite volume fraction f (in contrast to using the full b-value range), with the

841 estimated exchange rates r_n from neurites to the extracellular space remaining

842 consistent across both datasets.

843

844 *In vivo* exchange time across cortical ribbon

43

Correspondence to Hong-Hsi Lee

845   Interestingly, the measured exchange times exhibit spatial variability across the cortex,

846   showing a pattern akin to cortical myelination (Edwards et al., 2018; Marques et al.,

847   2017) derived from multimodality images, as well as to the previous *in vivo* NEXI study

848   (Uhl et al., 2024). Specifically, regions with higher levels of myelination, such as the

849   motor cortex, somatosensory cortex, visual cortex, transverse temporal gyrus, and

850   posterior part of the cingulate cortex, tend to display longer exchange times.

851   Additionally, there appears to be a spatial gradient of myelination increasing from the

852   anterior to the posterior parts of the cingulate cortex, consistent with the observed

853   pattern in the exchange time projection illustrated in Figure 8. Further investigation is

854   needed to elucidate the association between cortical myelination and

855   intercompartmental exchange times.

856

857   <u>Accelerating NEXI processing</u>

858   We have also demonstrated a significant acceleration of NEXI model fitting, achieving

859   over 100-fold increase in speed using the GPU-based askAdam framework while

860   maintaining comparable estimation performance. Our evaluation using the *in silico*

861   head phantom revealed that, although askAdam's estimation accuracy is slightly

862   reduced compared to voxel-wise NLLS fitting, the bias in exchange time introduced by

863   askAdam is small (difference on median=0.41 ms at SNR=50 between NLLS and

864   askAdam, Figure 4), particularly when considering inter-subject variability (Figure 8).

865   Another advantage of askAdam is its ability to integrate spatial regularization by

866   updating all microstructure parameters simultaneously during the fitting process. This

867   feature proves particularly beneficial when dealing with low SNR data. As a proof-of-

868   concept demonstration, we implemented 2D-TV regularization on the neurite volume

869   fraction parameter map (see Supplementary Figure S2). Yet, more advanced methods,

44

Correspondence to Hong-Hsi Lee

870   such as total generalized variation (TGV) (Bredies et al., 2010; Knoll et al., 2011) or

871   structure-guided TV (Ehrhardt and Betcke, 2016), can also be employed. These

872   methods have demonstrated better preservation of anatomical structures, which could

873   be important for cortical gray matter given its highly folded nature. Moreover, the

874   flexibility of askAdam's loss function allows spatial regularization to extend beyond a

875   single parameter map. It can be applied simultaneously across multi-parameter maps

876   along with other anatomical information, such as sharp edges in the image (Liu et al.,

877   2011). Despite spatial regularization may be useful in reducing the spatial variance

878   and stabilizing the estimation, caution should be exercised to determine the optimal

879   regularization parameter to prevent measurement bias resulting from over-

880   regularization (over-smoothing) that could potentially decrease the sensitivity of the

881   method in assessing specific pathologies, as diseased tissues often have greater

882   microstructural variations when compared to normal tissues. Nonetheless, spatial

883   regularization is only an optional feature of askAdam and can be disabled in the

884   optimization. As shown in Figure 8, the estimation performance without TV

885   regularization is nearly identical to the results obtained with TV regularization at the

886   group-level comparison. It is worth noting that the primary benefit of utilizing the

887   'askAdam' framework lies in its computation time efficiency. Since the estimation

888   principle is still based on minimizing the signal differences between a tissue model

889   and the measurement data, it will inherit similar degeneracy issues in ill-conditioned

890   parameter estimation as in NLLS voxel-wise approaches.

891

892   <u>Limitations</u>

893   Our study has some limitations. First, the NEXI model employed in our analysis does

894   not explicitly account for water diffusion within the soma. It is established that the soma
       45

       Correspondence to Hong-Hsi Lee

895   contributes approximately 10-20% of the water signal at low b-values in gray matter

896   (Olesen et al., 2022). At weak diffusion weighting, the signal contribution from the

897   soma may be non-negligible. We observed markedly shorter measured exchange

898   times when incorporating b=1 ms/µm^2 in the NEXI fitting (Supplementary Table S2).

899   The fit residuals also exhibited stronger systematic differences between the NEXI

900   forward signal and the measurements (see Supplementary Figure S6), prompting us

901   to include data with only b>1 ms/µm^2 for the NEXI fitting. Note that the *in vivo* data

902   demonstrated only weak time-dependence at b=1 ms/µm^2 (see Supplementary

903   Figures S5 and S6). This suggests that at the low diffusion weightings, it will be more

904   challenging to disentangle the exchange effect from diffusion. Expanding the NEXI

905   model to encompass a non-exchanging restricted compartment to represent the soma

906   could potentially alleviate signal discrepancies at low b-values (Olesen et al., 2022),

907   yet this would introduce additional model parameters that may compromise estimation

908   precision. On the other hand, signal originating from myelinated fibers in grey matter

909   that is not accounted for in the NEXI model, though comprising only a small portion

910   (Shapson-Coe et al., 2024), may become more pronounced at very high b-values (e.g.,

911   ≥17 ms/µm^2 for *in vivo*) and introduce biases in the NEXI estimation (Olesen et al.,

912   2022). An *ex vivo* mouse study at 16.4T by Olesen et al. demonstrated that the

913   differences in exchange time with and without considering the myelinated fiber were

914   between 0.3 ms and 0.9 ms with the measured exchange times between 3.9 ms and

915   5.8 ms. Whether these differences hold for *in vivo* imaging will need further

916   investigation. However, it will be particularly challenging to separate the myelinated

917   fiber signal from the unmyelinated neurite signal in grey matter *in vivo* human

918   experiments, considering the SNR and b-values demands. Other signal sources,

919   including microscopic kurtosis (Henriques et al., 2021), effects of the localization

    46

Correspondence to Hong-Hsi Lee

920   regime (Moutal and Grebenkov, 2020), effects of deviation from idealized geometries

921   (Ianus et al., 2021) and effects of dendritic spines (Palombo et al., 2017) among others,

922   that were not accounted for in the NEXI signal model may also contribute to the

923   exchange time biases we observed between the Connectome 1.0 and Connectome

924   2.0 protocols. While intra-vascular and extra-vascular signal was considered to be

925   highly suppressed due to the use of high b-value data here, the exchange effect

926   between these two compartments may also need to be considered when low b-value

927   (<1 ms/µm^2) data is used to fit the model with soma compartment.

928

929   Another limitation of NEXI is that the signal model does not account for the potential

930   transverse relaxation time differences between the two compartments. Several reports

931   have suggested that the intra-neurite transverse relaxation time is slightly longer than

932   that of the extra-cellular water (Gong et al., 2024; Lee et al., 2024; Veraart et al., 2018).

933   This difference can lead to an echo time dependence on the estimated neurite volume

934   fraction, thus introducing an additional study bias in the estimated exchange time when

935   different echo times are used in the acquisition. This effect may be alleviated by

936   incorporating the compartmental transverse relaxation rates in the NEXI model with

937   dMRI data acquired at multiple echo times (Lee et al., 2024). The additional

938   compartmental relaxation parameters may also provide extra insight into the

939   microstructure environment, but this will certainly lengthen the scan time of the existing

940   protocol due to additional data acquisition.

941

942   The drawback of including only higher b-value (>1 ms/µm^2) data is the reduced

943   sensitivity to estimate the neurite diffusivity. Previous works demonstrated that the

944   neurite diffusivity was about 2 µm^2/ms in white matter (Coelho et al., 2022; Dhital et

47

Correspondence to Hong-Hsi Lee

945   al., 2019) and gray matter (Ianuş et al., 2022; Palombo et al., 2020), which required

946   lower b-value data for a reliable estimation. This is in line with our simulation results

947   and *in vivo* data where the neurite diffusivity is the least robust estimated parameter

948   in the NEXI model given the current imaging protocols and often fitted to the upper

949   bound of the allowed range. Setting a higher fitting upper bound for neurite diffusivity

950   only shows minor impacts on the estimated exchange time (see Supplementary Figure

951   S3). Further investigation is necessary to accurately assess soma properties in

952   conjunction with the intercompartmental exchange effect.

953

954   The partial volume effect arising from the superficial white matter and CSF due to the

955   relatively large voxel size compared to cortical thickness can also affect the

956   measurement accuracy (our dMRI data: 2 mm isotropic vs typical cortical

957   thickness=2.2-2.9 mm across all ages (Frangou et al., 2022)). We examined the

958   potential impact of the partial volume effect in our data through correlation analysis

959   between the exchange time and cortical thickness and found no significant association

960   between the two parameters (Figure 9a). While this evidence may suggest that the

961   partial volume effect due to local white matter and CSF may not influence the

962   measured exchange time significantly, it is also possible that they could have an

963   opposite effect in the NEXI estimation. Further investigation is required to understand

964   how different tissue types (grey matter, white matter and CSF) coexist in a voxel may

965   impact the estimation of the *in vivo* NEXI exchange time. Increasing the spatial

966   resolution can mitigate the partial volume effect at the expense of reducing SNR and

967   lengthening scan time. Nevertheless, given the high-quality data provided by the

968   Connectome 2.0 scanner (SNR=55 at b=0 before denoising), obtaining high-resolution

969   dMRI while maintaining reasonable SNR using standard spin-echo EPI sequences
48

Correspondence to Hong-Hsi Lee

970 may be feasible. Alternatively, recent advancements in pulse sequence development

971 (Dong et al., 2024; Ramos-Llordén et al., 2020; Setsompop et al., 2018), denoising

972 (Henriques et al., 2023; Lemberskiy et al., 2023; Olesen et al., 2023), super-resolution

973 techniques (Coupé et al., 2013; H. H. Lee et al., 2019; Manjón et al., 2010) and

974 diffusion sampling strategy (Fan et al., 2017) for high-resolution diffusion imaging offer

975 a promising avenue to achieve high resolution with good SNR for gray matter imaging.

976 Another advantage of higher spatial resolution is the potential to investigate the

977 intercompartment exchange effect at multiple cortical depths, providing more specific

978 information reflecting tissue composition and arrangement across the cortical layers.

979

980 To be able to obtain high-quality data for NEXI exchange time mapping, we employed

981 a protocol comprising 15 b-values at 64 diffusion gradient directions from 3 diffusion

982 times, resulting in more than 80 min total acquisition time, which is clearly too long for

983 clinical applications. Reducing the number of diffusion gradient directions by half as

984 the protocol used for Connectome 1.0 and Connectome 2.0 comparison can shorten

985 the scan time to 40 min while retaining comparable results as the 64-direction high

986 SNR protocol. Future studies will focus on protocol optimization on sequence

987 parameters, such as diffusion times, b-values, and number of diffusion gradient

988 directions, to achieve a more accessible scan time (<20 min) for clinical and research

989 applications.

990

49

Correspondence to Hong-Hsi Lee

6. Conclusions

991   The ultra-high-gradient performance Connectome 2.0 scanner provides high-quality

993   data and greater flexibility in experimental design to measure intercompartmental

994   exchange effects between intracellular and extracellular water in the brain gray matter.

995   The *in vivo* intercompartmental exchange time was estimated to be about 13±8 ms

996   across the human cortex based on the anisotropic Kärger model. Our work further

997   indicated that addressing the Rician noise floor sufficiently, either in the signal model

998   or in the data processing, is crucial to measure the short exchange time ($\leq$20 ms) using

999   NEXI, especially when a short diffusion time cannot be easily deployed due to

1000   hardware constraints. The narrow pulse approximation in NEXI did not introduce

1001   significant bias in the exchange time measurements using (ultra-)high gradient

1002   performance MRI systems, such as Connectome 1.0 and 2.0 scanners, under clinically

1003   relevant SNR circumstances. Using the GPU-based askAdam processing pipeline, we

1004   accelerated the NEXI data fitting process by 100-fold. Our work provides additional

1005   insights and groundwork that may aid in NEXI protocol optimization for *in vivo* imaging

1006   in future studies.

1007

50

Correspondence to Hong-Hsi Lee

References

Ades-Aron, B., Veraart, J., Kochunov, P., McGuire, S., Sherman, P., Kellner, E., Novikov, D.S., Fieremans, E., 2018. Evaluation of the accuracy and precision of the diffusion parameter EStImation with Gibbs and NoisE removal pipeline. NeuroImage 183, 532–543. https://doi.org/10.1016/j.neuroimage.2018.07.066

Andersson, J.L.R., Skare, S., Ashburner, J., 2003. How to correct susceptibility distortions in spin-echo echo-planar images: application to diffusion tensor imaging. Neuroimage 20, 870–888. https://doi.org/10.1016/s1053-8119(03)00336-7

Andersson, J.L.R., Sotiropoulos, S.N., 2016. An integrated approach to correction for off-resonance effects and subject movement in diffusion MR imaging. Neuroimage 125, 1063–1078. https://doi.org/10.1016/j.neuroimage.2015.10.019

Åslund, I., Nowacka, A., Nilsson, M., Topgaard, D., 2009. Filter-exchange PGSE NMR determination of cell membrane permeability. J. Magn. Reson. 200, 291–295. https://doi.org/10.1016/j.jmr.2009.07.015

Assaf, Y., Blumenfeld-Katzir, T., Yovel, Y., Basser, P.J., 2008. Axcaliber: A method for measuring axon diameter distribution from diffusion MRI. Magn. Reson. Med. 59, 1347–1354. https://doi.org/10.1002/mrm.21577

Assaf, Y., Freidlin, R.Z., Rohde, G.K., Basser, P.J., 2004. New modeling and experimental framework to characterize hindered and restricted water diffusion in brain white matter. Magn. Reson. Med. 52, 965–978. https://doi.org/10.1002/mrm.20274

Avants, B.B., Tustison, N.J., Song, G., Cook, P.A., Klein, A., Gee, J.C., 2011. A reproducible evaluation of ANTs similarity metric performance in brain image registration. Neuroimage 54, 2033–2044. https://doi.org/10.1016/j.neuroimage.2010.09.025

Badaut, J., Fukuda, A.M., Jullienne, A., Petry, K.G., 2014. Aquaporin and brain diseases. Biochim. Biophys. Acta (BBA) - Gen. Subj. 1840, 1554–1565. https://doi.org/10.1016/j.bbagen.2013.10.032

Bai, R., Li, Z., Sun, C., Hsu, Y.-C., Liang, H., Basser, P., 2020. Feasibility of filter-exchange imaging (FEXI) in measuring different exchange processes in human brain. NeuroImage 219, 117039. https://doi.org/10.1016/j.neuroimage.2020.117039

51

Correspondence to Hong-Hsi Lee

1042 Bai, R., Springer, C.S., Plenz, D., Basser, P.J., 2019. Brain active transmembrane
1043   water cycling measured by MR is associated with neuronal activity. Magn. Reson.
1044   Med. 81, 1280–1295. https://doi.org/10.1002/mrm.27473

1045 Bai, R., Springer, C.S., Plenz, D., Basser, P.J., 2018. Fast, Na+/K+ pump driven,
1046   steady-state transcytolemmal water exchange in neuronal tissue: A study of rat
1047   brain cortical cultures. Magn. Reson. Med. 79, 3207–3217.
1048   https://doi.org/10.1002/mrm.26980

1049 Basser, P.J., 1997. New Histological and Physiological Stains Derived from
1050   Diffusion-Tensor MR Images. Ann. N. York Acad. Sci. 820, 123–138.
1051   https://doi.org/10.1111/j.1749-6632.1997.tb46192.x

1052 Beaulieu, C., 2002. The basis of anisotropic water diffusion in the nervous system - a
1053   technical review. NMR in biomedicine 15, 435–455.
1054   https://doi.org/10.1002/nbm.782

1055 Billot, B., Magdamo, C., Cheng, Y., Arnold, S.E., Das, S., Iglesias, J.E., 2023.
1056   Robust machine learning segmentation for large-scale analysis of heterogeneous
1057   clinical brain MRI datasets. Proc National Acad Sci 120, e2216399120.
1058   https://doi.org/10.1073/pnas.2216399120

1059 Bredies, K., Kunisch, K., Pock, T., 2010. Total Generalized Variation. SIAM J.
1060   Imaging Sci. 3, 492–526. https://doi.org/10.1137/090769521

1061 Cai, T.X., Benjamini, D., Komlosh, M.E., Basser, P.J., Williamson, N.H., 2018. Rapid
1062   detection of the presence of diffusion exchange. J. Magn. Reson. 297, 17–22.
1063   https://doi.org/10.1016/j.jmr.2018.10.004

1064 Cai, T.X., Williamson, N.H., Ravin, R., Basser, P.J., 2023. Multiexponential analysis
1065   of diffusion exchange times reveals a distinct exchange process associated with
1066   metabolic activity, in: Proceedings 31. Annual Meeting International Society for
1067   Magnetic Resonance in Medicine. Toronto, Canada, p. 5017.

1068 Callaghan, P.T., Furó, I., 2004. Diffusion-diffusion correlation and exchange as a
1069   signature for local order and dynamics. J. Chem. Phys. 120, 4032–4038.
1070   https://doi.org/10.1063/1.1642604

1071 Carr, H.Y., Purcell, E.M., 1954. Effects of Diffusion on Free Precession in Nuclear
1072   Magnetic Resonance Experiments. Phys. Rev. 94, 630–638.
1073   https://doi.org/10.1103/physrev.94.630

1074 Chakwizira, A., Zhu, A., Foo, T., Westin, C.-F., Szczepankiewicz, F., Nilsson, M.,
1075   2023. Diffusion MRI with free gradient waveforms on a high-performance gradient
1076   system: Probing restriction and exchange in the human brain. NeuroImage 283,
1077   120409. https://doi.org/10.1016/j.neuroimage.2023.120409

1078 Chan, K.-S., Kim, T.H., Bilgic, B., Marques, J.P., 2022. Semi-supervised learning for
1079   fast multi-compartment relaxometry myelin water imaging (MCR-MWI), in:

52

Correspondence to Hong-Hsi Lee

1080   Proceedings 30. Annual Meeting International Society for Magnetic Resonance in
1081   Medicine. London, United Kingdom, p. 1639. https://doi.org/10.58530/2022/1639

1082   Coelho, S., Baete, S.H., Lemberskiy, G., Ades-Aron, B., Barrol, G., Veraart, J.,
1083   Novikov, D.S., Fieremans, E., 2022. Reproducibility of the Standard Model of
1084   diffusion in white matter on clinical MRI systems. NeuroImage 257, 119290.
1085   https://doi.org/10.1016/j.neuroimage.2022.119290

1086   Coupé, P., Manjón, J.V., Chamberland, M., Descoteaux, M., Hiba, B., 2013.
1087   Collaborative patch-based super-resolution for diffusion-weighted images.
1088   NeuroImage 83, 245–261. https://doi.org/10.1016/j.neuroimage.2013.06.030

1089   Dhital, B., Reisert, M., Kellner, E., Kiselev, V.G., 2019. Intra-axonal diffusivity in brain
1090   white matter. NeuroImage 189, 543–550.
1091   https://doi.org/10.1016/j.neuroimage.2019.01.015

1092   Dong, Z., Reese, T.G., Lee, H.-H., Huang, S.Y., Polimeni, J.R., Wald, L.L., Wang, F.,
1093   2024. Romer-EPTI: Rotating-view motion-robust super-resolution EPTI for SNR-
1094   efficient distortion-free in-vivo mesoscale dMRI and microstructure imaging.
1095   bioRxiv 2024.01.26.577343. https://doi.org/10.1101/2024.01.26.577343

1096   Edwards, L.J., Kirilina, E., Mohammadi, S., Weiskopf, N., 2018. Microstructural
1097   imaging of human neocortex in vivo. Neuroimage 182, 184–206.
1098   https://doi.org/10.1016/j.neuroimage.2018.02.055

1099   Ehrhardt, M.J., Betcke, M.M., 2016. Multicontrast MRI Reconstruction with Structure-
1100   Guided Total Variation. SIAM J. Imaging Sci. 9, 1084–1106.
1101   https://doi.org/10.1137/15m1047325

1102   Eichner, C., Cauley, S.F., Cohen-Adad, J., Möller, H.E., Turner, R., Setsompop, K.,
1103   Wald, L.L., 2015. Real diffusion-weighted MRI enabling true signal averaging and
1104   increased diffusion contrast. NeuroImage 122, 373–384.
1105   https://doi.org/10.1016/j.neuroimage.2015.07.074

1106   Fan, Q., Nummenmaa, A., Polimeni, J.R., Witzel, T., Huang, S.Y., Wedeen, V.J.,
1107   Rosen, B.R., Wald, L.L., 2017. HIgh b-value and high Resolution Integrated
1108   Diffusion (HIBRID) imaging. NeuroImage 150, 162–176.
1109   https://doi.org/10.1016/j.neuroimage.2017.02.002

1110   Fan, Q., Nummenmaa, A., Witzel, T., Ohringer, N., Tian, Q., Setsompop, K.,
1111   Klawiter, E.C., Rosen, B.R., Wald, L.L., Huang, S.Y., 2020. Axon diameter index
1112   estimation independent of fiber orientation distribution using high-gradient
1113   diffusion MRI. NeuroImage 222, 117197.
1114   https://doi.org/10.1016/j.neuroimage.2020.117197

1115   Fan, Q., Witzel, T., Nummenmaa, A., Dijk, K.R.A.V., Horn, J.D.V., Drews, M.K.,
1116   Somerville, L.H., Sheridan, M.A., Santillana, R.M., Snyder, J., Hedden, T., Shaw,
1117   E.E., Hollinshead, M.O., Renvall, V., Zanzonico, R., Keil, B., Cauley, S., Polimeni,
1118   J.R., Tisdall, D., Buckner, R.L., Wedeen, V.J., Wald, L.L., Toga, A.W., Rosen,

53

Correspondence to Hong-Hsi Lee

1119 B.R., 2016. MGH–USC Human Connectome Project datasets with ultra-high b-
1120 value diffusion MRI. NeuroImage 124, 1108–1114.
1121 https://doi.org/10.1016/j.neuroimage.2015.08.075

1122 Feinberg, D.A., Beckett, A.J.S., Vu, A.T., Stockmann, J., Huber, L., Ma, S., Ahn, S.,
1123 Setsompop, K., Cao, X., Park, S., Liu, C., Wald, L.L., Polimeni, J.R., Mareyam, A.,
1124 Gruber, B., Stirnberg, R., Liao, C., Yacoub, E., Davids, M., Bell, P., Rummert, E.,
1125 Koehler, M., Potthast, A., Gonzalez-Insua, I., Stocker, S., Gunamony, S., Dietz,
1126 P., 2023. Next-generation MRI scanner designed for ultra-high-resolution human
1127 brain imaging at 7 Tesla. Nat. Methods 20, 2048–2057.
1128 https://doi.org/10.1038/s41592-023-02068-7

1129 Fieremans, E., Jensen, J.H., Helpern, J.A., 2011. White matter characterization with
1130 diffusional kurtosis imaging. Neuroimage 58, 177–188.
1131 https://doi.org/10.1016/j.neuroimage.2011.06.006

1132 Fieremans, E., Novikov, D.S., Jensen, J.H., Helpern, J.A., 2010. Monte Carlo study
1133 of a two-compartment exchange model of diffusion. NMR Biomed. 23, 711–724.
1134 https://doi.org/10.1002/nbm.1577

1135 Fischl, B., 2012. FreeSurfer. NeuroImage 62, 774–781.
1136 https://doi.org/10.1016/j.neuroimage.2012.01.021

1137 Foo, T.K.F., Tan, E.T., Vermilyea, M.E., Hua, Y., Fiveland, E.W., Piel, J.E., Park, K.,
1138 Ricci, J., Thompson, P.S., Graziani, D., Conte, G., Kagan, A., Bai, Y., Vasil, C.,
1139 Tarasek, M., Yeo, D.T.B., Snell, F., Lee, D., Dean, A., DeMarco, J.K., Shih, R.Y.,
1140 Hood, M.N., Chae, H., Ho, V.B., 2020. Highly efficient head-only magnetic field
1141 insert gradient coil for achieving simultaneous high gradient amplitude and slew
1142 rate at 3.0T (MAGNUS) for brain microstructure imaging. Magn. Reson. Med. 83,
1143 2356–2369. https://doi.org/10.1002/mrm.28087

1144 Frangou, S., Modabbernia, A., Williams, S.C.R., Papachristou, E., Doucet, G.E.,
1145 Agartz, I., Aghajani, M., Akudjedu, T.N., Albajes-Eizagirre, A., Alnæs, D., Alpert,
1146 K.I., Andersson, M., Andreasen, N.C., Andreassen, O.A., Asherson, P.,
1147 Banaschewski, T., Bargallo, N., Baumeister, S., Baur-Streubel, R., Bertolino, A.,
1148 Bonvino, A., Boomsma, D.I., Borgwardt, S., Bourque, J., Brandeis, D., Breier, A.,
1149 Brodaty, H., Brouwer, R.M., Buitelaar, J.K., Busatto, G.F., Buckner, R.L., Calhoun,
1150 V., Canales-Rodríguez, E.J., Cannon, D.M., Caseras, X., Castellanos, F.X.,
1151 Cervenka, S., Chaim-Avancini, T.M., Ching, C.R.K., Chubar, V., Clark, V.P.,
1152 Conrod, P., Conzelmann, A., Crespo-Facorro, B., Crivello, F., Crone, E.A., Dale,
1153 A.M., Dannlowski, U., Davey, C., Geus, E.J.C. de, Haan, L. de, Zubicaray, G.I. de,
1154 Braber, A. den, Dickie, E.W., Giorgio, A.D., Doan, N.T., Dørum, E.S., Ehrlich, S.,
1155 Erk, S., Espeseth, T., Fatouros-Bergman, H., Fisher, S.E., Fouche, J., Franke, B.,
1156 Frodl, T., Fuentes-Claramonte, P., Glahn, D.C., Gotlib, I.H., Grabe, H., Grimm, O.,
1157 Groenewold, N.A., Grotegerd, D., Gruber, O., Gruner, P., Gur, R.E., Gur, R.C.,
1158 Hahn, T., Harrison, B.J., Hartman, C.A., Hatton, S.N., Heinz, A., Heslenfeld, D.J.,
1159 Hibar, D.P., Hickie, I.B., Ho, B., Hoekstra, P.J., Hohmann, S., Holmes, A.J.,
1160 Hoogman, M., Hosten, N., Howells, F.M., Pol, H.E.H., Huyser, C., Jahanshad, N.,

54

Correspondence to Hong-Hsi Lee

1161 James, A., Jernigan, T.L., Jiang, J., Jönsson, E.G., Joska, J.A., Kahn, R., Kalnin,
1162 A., Kanai, R., Klein, M., Klyushnik, T.P., Koenders, L., Koops, S., Krämer, B.,
1163 Kuntsi, J., Lagopoulos, J., Lázaro, L., Lebedeva, I., Lee, W.H., Lesch, K.,
1164 Lochner, C., Machielsen, M.W.J., Maingault, S., Martin, N.G., Martínez-Zalacaín,
1165 I., Mataix-Cols, D., Mazoyer, B., McDonald, C., McDonald, B.C., McIntosh, A.M.,
1166 McMahon, K.L., McPhilemy, G., Meinert, S., Menchón, J.M., Medland, S.E.,
1167 Meyer-Lindenberg, A., Naaijen, J., Najt, P., Nakao, T., Nordvik, J.E., Nyberg, L.,
1168 Oosterlaan, J., Foz, V.O. de la, Paloyelis, Y., Pauli, P., Pergola, G., Pomarol-
1169 Clotet, E., Portella, M.J., Potkin, S.G., Radua, J., Reif, A., Rinker, D.A., Roffman,
1170 J.L., Rosa, P.G.P., Sacchet, M.D., Sachdev, P.S., Salvador, R., Sánchez-Juan,
1171 P., Sarró, S., Satterthwaite, T.D., Saykin, A.J., Serpa, M.H., Schmaal, L., Schnell,
1172 K., Schumann, G., Sim, K., Smoller, J.W., Sommer, I., Soriano-Mas, C., Stein,
1173 D.J., Strike, L.T., Swagerman, S.C., Tamnes, C.K., Temmingh, H.S.,
1174 Thomopoulos, S.I., Tomyshev, A.S., Tordesillas-Gutiérrez, D., Trollor, J.N.,
1175 Turner, J.A., Uhlmann, A., Heuvel, O.A. van den, Meer, D. van den, Wee, N.J.A.
1176 van der, Haren, N.E.M. van, Ent, D. van 't, Erp, T.G.M. van, Veer, I.M., Veltman,
1177 D.J., Voineskos, A., Völzke, H., Walter, H., Walton, E., Wang, L., Wang, Y.,
1178 Wassink, T.H., Weber, B., Wen, W., West, J.D., Westlye, L.T., Whalley, H.,
1179 Wierenga, L.M., Wittfeld, K., Wolf, D.H., Worker, A., Wright, M.J., Yang, K.,
1180 Yoncheva, Y., Zanetti, M.V., Ziegler, G.C., (KaSP), K.S.P., Thompson, P.M.,
1181 Dima, D., 2022. Cortical thickness across the lifespan: Data from 17,075 healthy
1182 individuals aged 3–90 years. Hum. Brain Mapp. 43, 431–451.
1183 https://doi.org/10.1002/hbm.25364

1184 Gong, T., Tax, C.M., Mancini, M., Jones, D.K., Zhang, H., Palombo, M., 2024. Multi-
1185 TE SANDI: Quantifying compartmental T2 relaxation times in the grey matter, in:
1186 Proceedings 32. Annual Meeting International Society for Magnetic Resonance in
1187 Medicine. p. 0766.

1188 Harms, R.L., Fritz, F.J., Tobisch, A., Goebel, R., Roebroeck, A., 2017. Robust and
1189 fast nonlinear optimization of diffusion MRI microstructure models. NeuroImage
1190 155, 82–96. https://doi.org/10.1016/j.neuroimage.2017.04.064

1191 Henriques, R.N., Ianuş, A., Novello, L., Jovicich, J., Jespersen, S.N., Shemesh, N.,
1192 2023. Efficient PCA denoising of spatially correlated redundant MRI data. Imaging
1193 Neurosci. 1, 1–26. https://doi.org/10.1162/imag_a_00049

1194 Henriques, R.N., Jespersen, S.N., Shemesh, N., 2021. Evidence for microscopic
1195 kurtosis in neural tissue revealed by correlation tensor MRI. Magn. Reson. Med.
1196 86, 3111–3130. https://doi.org/10.1002/mrm.28938

1197 Hernandez-Fernandez, M., Reguly, I., Jbabdi, S., Giles, M., Smith, S., Sotiropoulos,
1198 S.N., 2019. Using GPUs to accelerate computational diffusion MRI: From
1199 microstructure estimation to tractography and connectomes. NeuroImage 188,
1200 598–615. https://doi.org/10.1016/j.neuroimage.2018.12.015

1201 Huang, S.Y., Tian, Q., Fan, Q., Witzel, T., Wichtmann, B., McNab, J.A., Bireley, J.D.,
1202 Machado, N., Klawiter, E.C., Mekkaoui, C., Wald, L.L., Nummenmaa, A., 2020.
1203 High-gradient diffusion MRI reveals distinct estimates of axon diameter index

55

Correspondence to Hong-Hsi Lee

within different white matter tracts in the in vivo human brain. Brain Struct. Funct. 225, 1277–1291. https://doi.org/10.1007/s00429-019-01961-2

Huang, S.Y., Witzel, T., Keil, B., Scholz, A., Davids, M., Dietz, P., Rummert, E., Ramb, R., Kirsch, J.E., Yendiki, A., Fan, Q., Tian, Q., Ramos-Llordén, G., Lee, H.-H., Nummenmaa, A., Bilgic, B., Setsompop, K., Wang, F., Avram, A.V., Komlosh, M., Benjamini, D., Magdoom, K.N., Pathak, S., Schneider, W., Novikov, D.S., Fieremans, E., Tounekti, S., Mekkaoui, C., Augustinack, J., Berger, D., Shapson-Coe, A., Lichtman, J., Basser, P.J., Wald, L.L., Rosen, B.R., 2021. Connectome 2.0: Developing the next-generation ultra-high gradient strength human MRI scanner for bridging studies of the micro-, meso- and macro-connectome. NeuroImage 243, 118530. https://doi.org/10.1016/j.neuroimage.2021.118530

Ianus, A., Alexander, D.C., Zhang, H., Palombo, M., 2021. Mapping complex cell morphology in the grey matter with double diffusion encoding MR: A simulation study. Neuroimage 241, 118424. https://doi.org/10.1016/j.neuroimage.2021.118424

Ianuş, A., Carvalho, J., Fernandes, F.F., Cruz, R., Chavarrias, C., Palombo, M., Shemesh, N., 2022. Soma and Neurite Density MRI (SANDI) of the in-vivo mouse brain and comparison with the Allen Brain Atlas. NeuroImage 254, 119135. https://doi.org/10.1016/j.neuroimage.2022.119135

Jelescu, I.O., Skowronski, A. de, Geffroy, F., Palombo, M., Novikov, D.S., 2022. Neurite Exchange Imaging (NEXI): A minimal model of diffusion in gray matter with inter-compartment water exchange. Neuroimage 256, 119277. https://doi.org/10.1016/j.neuroimage.2022.119277

Jespersen, S.N., Kroenke, C.D., Østergaard, L., Ackerman, J.J.H., Yablonskiy, D.A., 2007. Modeling dendrite density from magnetic resonance diffusion measurements. Neuroimage 34, 1473–1486. https://doi.org/10.1016/j.neuroimage.2006.10.037

Jovicich, J., Czanner, S., Greve, D., Haley, E., Kouwe, A. van der, Gollub, R., Kennedy, D., Schmitt, F., Brown, G., MacFall, J., Fischl, B., Dale, A., 2006. Reliability in multi-site structural MRI studies: Effects of gradient non-linearity correction on phantom and human data. NeuroImage 30, 436–443. https://doi.org/10.1016/j.neuroimage.2005.09.046

Jung, S., Lee, H., Ryu, K., Song, J.E., Park, M., Moon, W., Kim, D., 2021. Artificial neural network for multi-echo gradient echo–based myelin water fraction estimation. Magnet Reson Med 85, 380–389. https://doi.org/10.1002/mrm.28407

Kaden, E., Kelm, N.D., Carson, R.P., Does, M.D., Alexander, D.C., 2016. Multi-compartment microscopic diffusion imaging. Neuroimage 139, 346–359. https://doi.org/10.1016/j.neuroimage.2016.06.002

Kärger, J., 1985. NMR self-diffusion studies in heterogeneous systems. Adv. Colloid Interface Sci. 23, 129–148. https://doi.org/10.1016/0001-8686(85)80018-x

56

Correspondence to Hong-Hsi Lee

1244   Kellner, E., Dhital, B., Kiselev, V.G., Reisert, M., 2016. Gibbs-ringing artifact removal
1245   based on local subvoxel-shifts. Magnetic resonance in medicine 76, 1574–1581.
1246   https://doi.org/10.1002/mrm.26054

1247   Khateri, M., Reisert, M., Sierra, A., Tohka, J., Kiselev, V.G., 2022. What does FEXI
1248   measure? NMR Biomed. 35, e4804. https://doi.org/10.1002/nbm.4804

1249   King, L.S., Kozono, D., Agre, P., 2004. From structure to disease: the evolving tale of
1250   aquaporin biology. Nat. Rev. Mol. Cell Biol. 5, 687–698.
1251   https://doi.org/10.1038/nrm1469

1252   Kingma, D.P., Ba, J., 2014. Adam: A Method for Stochastic Optimization. arXiv.
1253   https://doi.org/10.48550/arxiv.1412.6980

1254   Klein, A., Tourville, J., 2012. 101 Labeled Brain Images and a Consistent Human
1255   Cortical Labeling Protocol. Front. Neurosci. 6, 171.
1256   https://doi.org/10.3389/fnins.2012.00171

1257   Knoll, F., Bredies, K., Pock, T., Stollberger, R., 2011. Second order total generalized
1258   variation (TGV) for MRI. Magn. Reson. Med. 65, 480–491.
1259   https://doi.org/10.1002/mrm.22595

1260   Lampinen, B., Lätt, J., Wasselius, J., Westen, D. van, Nilsson, M., 2021. Time
1261   dependence in diffusion MRI predicts tissue outcome in ischemic stroke patients.
1262   Magn. Reson. Med. 86, 754–764. https://doi.org/10.1002/mrm.28743

1263   Lasič, S., Nilsson, M., Lätt, J., Ståhlberg, F., Topgaard, D., 2011. Apparent exchange
1264   rate mapping with diffusion MRI. Magn. Reson. Med. 66, 356–365.
1265   https://doi.org/10.1002/mrm.22782

1266   Lätt, J., Nilsson, M., Westen, D. van, Wirestam, R., Ståhlberg, F., Brockstedt, S.,
1267   2009. Diffusion-weighted MRI measurements on stroke patients reveal water-
1268   exchange mechanisms in sub-acute ischaemic lesions. NMR Biomed. 22, 619–
1269   628. https://doi.org/10.1002/nbm.1376

1270   Le Bihan, D., 1995. Molecular diffusion, tissue microdynamics and microstructure.
1271   NMR Biomed. 8, 375–386. https://doi.org/10.1002/nbm.1940080711

1272   Lee, H.-H., Chan, K.S., Llorden, G.R., Huang, S.Y., 2024. TENEXI: Echo time-
1273   dependent neurite exchange imaging for in vivo evaluation of exchange time and
1274   relaxation time on the Connectome 2.0 scanner, in: Proceedings 32. Annual
1275   Meeting International Society for Magnetic Resonance in Medicine. p. 3468.

1276   Lee, H.H., Lin, Y.C., Lemberskiy, G., Ades-Aron, B., Baete, S., Boada, F.E.,
1277   Fieremans, E., Novikov, D.S., 2019. SUper-REsolution TRACTography (SURE-
1278   TRACT) pipeline using self-similarity between diffusional and anatomical images,
1279   in: Proceedings 27. Annual Meeting International Society for Magnetic Resonance
1280   in Medicine. Montreal, Canada, p. 0167.

Correspondence to Hong-Hsi Lee

1281 Lee, H.H., Olesen, J.L., Tian, Q., Llorden, G.R., Jespersen, S.N., Huang, S.Y., 2022.
1282   Revealing diffusion time-dependence and exchange effect in the in vivo human
1283   brain gray matter by using high gradient diffusion MRI, in: Proceedings 30. Annual
1284   Meeting International Society for Magnetic Resonance in Medicine. London,
1285   United Kingdom, p. 0254. https://doi.org/10.58530/2022/0254

1286 Lee, H.-H., Papaioannou, A., Novikov, D.S., Fieremans, E., 2020. In vivo observation
1287   and biophysical interpretation of time-dependent diffusion in human cortical gray
1288   matter. Neuroimage 222, 117054.
1289   https://doi.org/10.1016/j.neuroimage.2020.117054

1290 Lee, J., Lee, D., Choi, J.Y., Shin, D., Shin, H., Lee, Jongho, 2019. Artificial neural
1291   network for myelin water imaging. Magn. Reson. Med. 83, 1875–1883.
1292   https://doi.org/10.1002/mrm.28038

1293 Lemberskiy, G., Chandarana, H., Bruno, M., Ginocchio, L.A., Huang, C., Tong, A.,
1294   Keerthivasan, M.B., Fieremans, E., Novikov, D.S., 2023. Feasibility of Accelerated
1295   Prostate Diffusion-Weighted Imaging on 0.55 T MRI Enabled With Random Matrix
1296   Theory Denoising. Investig. Radiol. 58, 720–729.
1297   https://doi.org/10.1097/rli.0000000000000979

1298 Li, C., Fieremans, E., Novikov, D.S., Ge, Y., Zhang, J., 2023. Measuring water
1299   exchange on a preclinical MRI system using filter exchange and diffusion time
1300   dependent kurtosis imaging. Magn. Reson. Med. 89, 1441–1455.
1301   https://doi.org/10.1002/mrm.29536

1302 Liu, T., Liu, J., Rochefort, L. de, Spincemaille, P., Khalidov, I., Ledoux, J.R., Wang,
1303   Y., 2011. Morphology enabled dipole inversion (MEDI) from a single-angle
1304   acquisition: Comparison with COSMOS in human brain imaging. Magnetic
1305   resonance in medicine 66, 777–783. https://doi.org/10.1002/mrm.22816

1306 Ma, D., Gulani, V., Seiberlich, N., Liu, K., Sunshine, J.L., Duerk, J.L., Griswold, M.A.,
1307   2013. Magnetic resonance fingerprinting. Nature 495, 187–192.
1308   https://doi.org/10.1038/nature11971

1309 MacAulay, N., 2021. Molecular mechanisms of brain water transport. Nat. Rev.
1310   Neurosci. 22, 326–344. https://doi.org/10.1038/s41583-021-00454-8

1311 Mahmutovic, M., Shrestha, M., Ramos-Llordén, G., Scholz, A., Kirsch, J.E., Wald,
1312   L.L., Möller, H.E., Mekkaoui, C., Huang, S.Y., Keil, B., 2024. A 72-channel Head
1313   Coil with an Integrated 16-Channel Field Camera for the Connectome 2.0
1314   Scanner, in: Proceedings 32. Annual Meeting International Society for Magnetic
1315   Resonance in Medicine. Singapore, p. 1030.

1316 Manjón, J.V., Coupé, P., Buades, A., Collins, D.L., Robles, M., 2010. MRI
1317   Superresolution Using Self-Similarity and Image Priors. Int. J. Biomed. Imaging
1318   2010, 425891. https://doi.org/10.1155/2010/425891

58

Correspondence to Hong-Hsi Lee

Marques, J.P., Hollander, D.D., Norris, D.G., Chan, K.-S., 2023. Improved R2* and QSM mapping for dummies - ask Adam, in: Proceedings 31. Annual Meeting International Society for Magnetic Resonance in Medicine. Toronto, Canada, p. 1089.

Marques, J.P., Khabipova, D., Gruetter, R., 2017. Studying cyto and myeloarchitecture of the human cortex at ultra-high field with quantitative imaging: R1, R2 * and magnetic susceptibility. NeuroImage 147, 152–163. https://doi.org/10.1016/j.neuroimage.2016.12.009

Martins, J.P. de A., Nilsson, M., Lampinen, B., Palombo, M., While, P.T., Westin, C.-F., Szczepankiewicz, F., 2021. Neural networks for parameter estimation in microstructural MRI: Application to a diffusion-relaxation model of white matter. NeuroImage 244, 118601. https://doi.org/10.1016/j.neuroimage.2021.118601

Moutal, N., Grebenkov, D.S., 2020. The localization regime in a nutshell. J. Magn. Reson. 320, 106836. https://doi.org/10.1016/j.jmr.2020.106836

Nedjati-Gilani, G.L., Schneider, T., Hall, M.G., Cawley, N., Hill, I., Ciccarelli, O., Drobnjak, I., Wheeler-Kingshott, C.A.M.G., Alexander, D.C., 2017. Machine learning based compartment models with permeability for white matter microstructure imaging. NeuroImage 150, 119–135. https://doi.org/10.1016/j.neuroimage.2017.02.013

Nilsson, M., Lätt, J., Westen, D. van, Brockstedt, S., Lasič, S., Ståhlberg, F., Topgaard, D., 2013. Noninvasive mapping of water diffusional exchange in the human brain using filter-exchange imaging. Magn. Reson. Med. 69, 1572–1580. https://doi.org/10.1002/mrm.24395

Ning, L., Nilsson, M., Lasič, S., Westin, C.-F., Rathi, Y., 2018. Cumulant expansions for measuring water exchange using diffusion MRI. J. Chem. Phys. 148, 074109. https://doi.org/10.1063/1.5014044

Novikov, D.S., Fieremans, E., Jespersen, S.N., Kiselev, V.G., 2019. Quantifying brain microstructure with diffusion MRI: Theory and parameter estimation. NMR Biomed. 32, e3998. https://doi.org/10.1002/nbm.3998

Novikov, D.S., Kiselev, V.G., Jespersen, S.N., 2018a. On modeling. Magnet Reson Med 79, 3172–3193. https://doi.org/10.1002/mrm.27101

Novikov, D.S., Veraart, J., Jelescu, I.O., Fieremans, E., 2018b. Rotationally-invariant mapping of scalar and orientational metrics of neuronal microstructure with diffusion MRI. NeuroImage 174, 518–538. https://doi.org/10.1016/j.neuroimage.2018.03.006

Olesen, J.L., Ianus, A., Østergaard, L., Shemesh, N., Jespersen, S.N., 2023. Tensor denoising of multidimensional MRI data. Magn. Reson. Med. 89, 1160–1172. https://doi.org/10.1002/mrm.29478

59

Correspondence to Hong-Hsi Lee

Olesen, J.L., Østergaard, L., Shemesh, N., Jespersen, S.N., 2022. Diffusion time dependence, power-law scaling, and exchange in gray matter. Neuroimage 251, 118976. https://doi.org/10.1016/j.neuroimage.2022.118976

Orton, M.R., Collins, D.J., Koh, D., Leach, M.O., 2014. Improved intravoxel incoherent motion analysis of diffusion weighted imaging by data driven Bayesian modeling. Magn. Reson. Med. 71, 411–420. https://doi.org/10.1002/mrm.24649

Palombo, M., Ianus, A., Guerreri, M., Nunes, D., Alexander, D.C., Shemesh, N., Zhang, H., 2020. SANDI: A compartment-based model for non-invasive apparent soma and neurite imaging by diffusion MRI. Neuroimage 215, 116835. https://doi.org/10.1016/j.neuroimage.2020.116835

Palombo, M., Ligneul, C., Hernandez-Garzon, E., Valette, J., 2017. Can we detect the effect of spines and leaflets on the diffusion of brain intracellular metabolites? Neuroimage 182, 283–293. https://doi.org/10.1016/j.neuroimage.2017.05.003

Papadopoulos, M.C., Verkman, A.S., 2013. Aquaporin water channels in the nervous system. Nat. Rev. Neurosci. 14, 265–277. https://doi.org/10.1038/nrn3468

Pasternak, O., Assaf, Y., Intrator, N., Sochen, N., 2008. Variational multiple-tensor fitting of fiber-ambiguous diffusion-weighted magnetic resonance imaging voxels. Magn. Reson. Imaging 26, 1133–1144. https://doi.org/10.1016/j.mri.2008.01.006

QSM Consensus Organization Committee, Bilgic, B., Costagli, M., Chan, K., Duyn, J., Langkammer, C., Lee, J., Li, X., Liu, C., Marques, J.P., Milovic, C., Robinson, S.D., Schweser, F., Shmueli, K., Spincemaille, P., Straub, S., Zijl, P. van, Wang, Y., ISMRM Electro-Magnetic Tissue Properties Study Group, 2024. Recommended implementation of quantitative susceptibility mapping for clinical research in the brain: A consensus of the ISMRM electro-magnetic tissue properties study group. Magn. Reson. Med. 91, 1834–1862. https://doi.org/10.1002/mrm.30006

Ramos-Llordén, G., Ning, L., Liao, C., Mukhometzianov, R., Michailovich, O., Setsompop, K., Rathi, Y., 2020. High-fidelity, accelerated whole-brain submillimeter in vivo diffusion MRI using gSlider-spherical ridgelets (gSlider-SR). Magn. Reson. Med. 84, 1781–1795. https://doi.org/10.1002/mrm.28232

Reisert, M., Kellner, E., Dhital, B., Hennig, J., Kiselev, V.G., 2017. Disentangling micro from mesostructure by diffusion MRI: A Bayesian approach. NeuroImage 147, 964–975. https://doi.org/10.1016/j.neuroimage.2016.09.058

Setsompop, K., Fan, Q., Stockmann, J., Bilgic, B., Huang, S., Cauley, S.F., Nummenmaa, A., Wang, F., Rathi, Y., Witzel, T., Wald, L.L., 2018. High-resolution in vivo diffusion imaging of the human brain with generalized slice dithered enhanced resolution: Simultaneous multislice (gSlider-SMS). Magn. Reson. Med. 79, 141–151. https://doi.org/10.1002/mrm.26653

60

Correspondence to Hong-Hsi Lee

Setsompop, K., Kimmlingen, R., Eberlein, E., Witzel, T., Cohen-Adad, J., McNab, J.A., Keil, B., Tisdall, M.D., Hoecht, P., Dietz, P., Cauley, S.F., Tountcheva, V., Matschl, V., Lenz, V.H., Heberlein, K., Potthast, A., Thein, H., Horn, J.V., Toga, A., Schmitt, F., Lehne, D., Rosen, B.R., Wedeen, V., Wald, L.L., 2013. Pushing the limits of in vivo diffusion MRI for the Human Connectome Project. Neuroimage 80, 220–233. https://doi.org/10.1016/j.neuroimage.2013.05.078

Shapson-Coe, A., Januszewski, M., Berger, D.R., Pope, A., Wu, Y., Blakely, T., Schalek, R.L., Li, P.H., Wang, S., Maitin-Shepard, J., Karlupia, N., Dorkenwald, S., Sjostedt, E., Leavitt, L., Lee, D., Troidl, J., Collman, F., Bailey, L., Fitzmaurice, A., Kar, R., Field, B., Wu, H., Wagner-Carena, J., Aley, D., Lau, J., Lin, Z., Wei, D., Pfister, H., Peleg, A., Jain, V., Lichtman, J.W., 2024. A petavoxel fragment of human cerebral cortex reconstructed at nanoscale resolution. Science 384, eadk4858. https://doi.org/10.1126/science.adk4858

Springer, C.S., Baker, E.M., Li, X., Moloney, B., Pike, M.M., Wilson, G.J., Anderson, V.C., Sammi, M.K., Garzotto, M.G., Kopp, R.P., Coakley, F.V., Rooney, W.D., Maki, J.H., 2023a. Metabolic activity diffusion imaging (MADI): II. Noninvasive, high-resolution human brain mapping of sodium pump flux and cell metrics. NMR Biomed. 36, e4782. https://doi.org/10.1002/nbm.4782

Springer, C.S., Baker, E.M., Li, X., Moloney, B., Wilson, G.J., Pike, M.M., Barbara, T.M., Rooney, W.D., Maki, J.H., 2023b. Metabolic activity diffusion imaging (MADI): I. Metabolic, cytometric modeling and simulations. NMR Biomed. 36, e4781. https://doi.org/10.1002/nbm.4781

Stejskal, E.O., Tanner, J.E., 1965. Spin Diffusion Measurements: Spin Echoes in the Presence of a Time-Dependent Field Gradient. J Chem Phys 42, 288–292. https://doi.org/10.1063/1.1695690

Tian, Q., Fan, Q., Witzel, T., Polackal, M.N., Ohringer, N.A., Ngamsombat, C., Russo, A.W., Machado, N., Brewer, K., Wang, F., Setsompop, K., Polimeni, J.R., Keil, B., Wald, L.L., Rosen, B.R., Klawiter, E.C., Nummenmaa, A., Huang, S.Y., 2022. Comprehensive diffusion MRI dataset for in vivo human brain microstructure mapping using 300 mT/m gradients. Sci. Data 9, 7. https://doi.org/10.1038/s41597-021-01092-6

Tournier, J.-D., Jeurissen, B., Christiaens, D., 2023. Iterative model-based Rician bias correction and its application to denoising in diffusion MRI, in: Proceedings 31. Annual Meeting International Society for Magnetic Resonance in Medicine. Toronto, Canada, p. 3795.

Tournier, J.-D., Smith, R., Raffelt, D., Tabbara, R., Dhollander, T., Pietsch, M., Christiaens, D., Jeurissen, B., Yeh, C.-H., Connelly, A., 2019. MRtrix3: A fast, flexible and open software framework for medical image processing and visualisation. Neuroimage 202, 116137. https://doi.org/10.1016/j.neuroimage.2019.116137

Correspondence to Hong-Hsi Lee

1435 Uhl, Q., Pavan, T., Molendowska, M., Jones, D.K., Palombo, M., Jelescu, I.O., 2024.
1436   Quantifying human gray matter microstructure using neurite exchange imaging
1437   (NEXI) and 300 mT/m gradients. Imaging Neurosci. 2, 1–19.
1438   https://doi.org/10.1162/imag_a_00104

1439 Veraart, J., Fieremans, E., Novikov, D.S., 2019. On the scaling behavior of water
1440   diffusion in human brain white matter. NeuroImage 185, 379–387.
1441   https://doi.org/10.1016/j.neuroimage.2018.09.075

1442 Veraart, J., Novikov, D.S., Christiaens, D., Ades-aron, B., Sijbers, J., Fieremans, E.,
1443   2016. Denoising of diffusion MRI using random matrix theory. Neuroimage 142,
1444   394–406. https://doi.org/10.1016/j.neuroimage.2016.08.016

1445 Veraart, J., Novikov, D.S., Fieremans, E., 2018. TE dependent Diffusion Imaging
1446   (TEdDI) distinguishes between compartmental T 2 relaxation times. NeuroImage
1447   182, 360–369. https://doi.org/10.1016/j.neuroimage.2017.09.030

1448 Veraart, J., Nunes, D., Rudrapatna, U., Fieremans, E., Jones, D.K., Novikov, D.S.,
1449   Shemesh, N., 2020. Nonivasive quantification of axon radii using diffusion MRI.
1450   Elife 9, e49855. https://doi.org/10.7554/elife.49855

1451 Weiger, M., Overweg, J., Rösler, M.B., Froidevaux, R., Hennel, F., Wilm, B.J., Penn,
1452   A., Sturzenegger, U., Schuth, W., Mathlener, M., Borgo, M., Börnert, P., Leussler,
1453   C., Luechinger, R., Dietrich, B.E., Reber, J., Brunner, D.O., Schmid, T., Vionnet,
1454   L., Pruessmann, K.P., 2018. A high-performance gradient insert for rapid and
1455   short-T2 imaging at full duty cycle. Magn. Reson. Med. 79, 3256–3266.
1456   https://doi.org/10.1002/mrm.26954

1457 Williamson, N.H., Ravin, R., Benjamini, D., Merkle, H., Falgairolle, M., O'Donovan,
1458   M.J., Blivis, D., Ide, D., Cai, T.X., Ghorashi, N.S., Bai, R., Basser, P.J., 2019.
1459   Magnetic resonance measurements of cellular and sub-cellular membrane
1460   structures in live and fixed neural tissue. eLife 8, e51101.
1461   https://doi.org/10.7554/elife.51101

1462 Williamson, N.H., Ravin, R., Cai, T.X., Benjamini, D., Falgairolle, M., O'Donovan,
1463   M.J., Basser, P.J., 2020. Real-time measurement of diffusion exchange rate in
1464   biological tissue. J. Magn. Reson. 317, 106782.
1465   https://doi.org/10.1016/j.jmr.2020.106782

1466 Williamson, N.H., Ravin, R., Cai, T.X., Falgairolle, M., O'Donovan, M.J., Basser, P.J.,
1467   2023. Water exchange rates measure active transport and homeostasis in neural
1468   tissue. PNAS Nexus 2, pgad056. https://doi.org/10.1093/pnasnexus/pgad056

1469 Zhang, H., Schneider, T., Wheeler-Kingshott, C.A., Alexander, D.C., 2012. NODDI:
1470   practical in vivo neurite orientation dispersion and density imaging of the human
1471   brain. Neuroimage 61, 1000–1016.
1472   https://doi.org/10.1016/j.neuroimage.2012.03.072

62

Correspondence to Hong-Hsi Lee

1473   Zimmerman, J.R., Brittin, W.E., 1957. Nuclear Magnetic Resonance Studies in
1474   Multiple Phase Systems: Lifetime of a Water Molecule in an Adsorbing Phase on
1475   Silica Gel. J. Phys. Chem. 61, 1328–1333. https://doi.org/10.1021/j150556a015

1476

1477

63

Correspondence to Hong-Hsi Lee

Data and Code Availability

The data and code that support the findings of this study will be made available upon reasonable request. The GPU processing tool for the ordinary NEXI model and NEXI with Rician mean model parameter estimation is available at https://github.com/kschan0214/gacelle.

Author Contributions

Kwok-Shing Chan: Conceptualization, Methodology, Software, Validation, Formal analysis, Investigation, Writing, Visualization

Yixin Ma: Investigation, Writing

Hansol Lee: Investigation, Writing

José P. Marques: Software, Conceptualization, Writing

Jonas Olesen: Software, Conceptualization, Methodology

Santiago Coelho: Conceptualization, Methodology, Writing

Dmitry S Novikov: Conceptualization, Methodology, Writing

Sune Jespersen: Software, Conceptualization, Methodology, Writing

Susie Y. Huang: Conceptualization, Methodology, Writing, Supervision, Funding acquisition

Hong-Hsi Lee: Conceptualization, Methodology, Software, Writing, Supervision, Funding acquisition

64

Correspondence to Hong-Hsi Lee

Declaration of Competing Interests

The authors have no competing interests related to the findings of this work.

Acknowledgements

Correspondence to Hong-Hsi Lee